Monthly Notices
of the
ROYAL ASTRONOMICAL SOCIETY

MNRAS **543,** 3628–3648 (2025) https://doi.org/10.1093/mnras/staf1587
Advance Access publication 2025 September 18

The impact of rotational mixing in intermediate-age star clusters with extended main-sequence turn-offs and extended red clumps

L. Martinelli[1,★] A. Miglio[2,3] G. Buldgen,[4] H. Schunker[1] C. Georgy[5] G. Cordoni[6]
K. Brogaard[2,7] P. Eggenberger[5] and E. Farrell[5]

[1]*School of Information and Physical Sciences, University of Newcastle, University Dr, Callaghan, NSW 2308, Australia*
[2]*Dipartimento di Fisica e Astronomia, Università degli Studi di Bologna, via Gobetti 93/2, I-40129 Bologna, Italy*
[3]*INAF – Osservatorio di Astrofisica e Scienza dello Spazio di Bologna, via Gobetti 93/3, I-40129 Bologna, Italy*
[4]*STAR Institute, Université de Liège, 19C Allée du 6 Août, 4000 Liège, Belgium*
[5]*Département d'astronomie, Université de Genève, Chemin Pegasi 51, CH-1290 Versoix, Switzerland*
[6]*Research School of Astronomy and Astrophysics, The Australian National University, Canberra, ACT 2611, Australia*
[7]*Stellar Astrophysics Centre, Department of Physics & Astronomy, Aarhus University, Ny Munkegade 120, DK-8000 Aarhus C, Denmark*

Accepted 2025 September 15. Received 2025 September 15; in original form 2025 June 9

ABSTRACT

The extended main-sequence turn-offs (eMSTOs) and extended red clumps (eRCs) observed in intermediate-age star clusters challenge the traditional understanding of clusters as simple stellar populations. Recently, eMSTOs have been interpreted as signatures of stellar rotation. In this work, we test the effectiveness of rotational mixing in shaping the colour–magnitude diagram (CMD) of star clusters. We computed a set of separate single-age synthetic stellar populations, referred to as 'Base Stellar Populations' (BSPs), including stellar rotation. These BSPs were generated from two grids of stellar models that share the same input physics but differ in the efficiency of rotational mixing. We used an optimization algorithm to determine the best combination of BSPs to fit the CMDs of two star clusters: the Small Magellanic Cloud cluster NGC 419 and the Milky Way cluster NGC 1817. The synthetic clusters with weak rotational mixing provide the best fit to both the eMSTO and eRC features for both clusters, and are consistent with the luminosities and asteroseismic masses we derived for eRC stars in NGC 1817. In contrast, synthetic clusters with strong rotational mixing result in overly bright post-main-sequence stars, inconsistent with observations. This suggests that, for intermediate-mass stars, the influence of rotational mixing of chemical elements on stellar evolution cannot be so strong as to significantly increase the post-main-sequence luminosity. A simple test suggests that accounting for self-extinction by decretion discs in equator-on fast rotators could influence inferred rotation distributions and help reconcile the projected rotational velocity discrepancy across the eMSTO between models and observations.

Key words: stars: evolution – Hertzsprung–Russell and colour–magnitude diagrams – stars: rotation – open clusters and associations: general – Magellanic Clouds – galaxies: star clusters: general.

1 INTRODUCTION

In the last two decades, high-precision *Hubble Space Telescope* (*HST*) photometry of star clusters has revealed that the colour–magnitude diagram (CMD) of most clusters in the Magellanic Clouds younger than ∼2.5 Gyr exhibit extended main-sequence turn-offs (eMSTOs; Milone et al. 2009, 2023a; Rubele, Kerber & Girardi 2010; Girardi et al. 2013), with some also displaying extended (or dual) red clumps (eRCs) (Girardi, Rubele & Kerber 2009; Milone et al. 2009). More recently, high-precision astrometric and photometric data from the *Gaia* mission (Gaia Collaboration 2018, 2021, 2023) have shown that these features are also present in many Galactic open clusters (Cordoni et al. 2018, 2024; Sun et al. 2019). These features are observed in clusters of both the Magellanic Clouds and the Milky Way, suggesting a shared underlying physical cause (Li et al. 2024).

The origin of the eMSTO was initially attributed to an age spread (on the order of hundreds of Myr) within the stellar populations of these clusters. This scenario also accounts for the presence of eRCs in some clusters (Rubele et al. 2010; Girardi et al. 2013), since a spread in age corresponds to a spread of mass among the stars in the same evolutionary phase.

However, the age spread scenario directly challenges the conventional understanding of star formation. Initial stellar feedback is expected to rapidly disperse surrounding gas (e.g. Krumholz 2014), and star formation in a typical $\sim10^5\,\mathrm{M}_\odot$ star cluster should conclude in $\lesssim10^7$ yr (Elmegreen & Efremov 1997) and so an age spread of hundreds of Myr is not expected. Although scenarios involving mergers between star clusters with different ages, or between a cluster and a giant molecular cloud have been proposed to account for age spreads (Bekki & Mackey 2009), they are expected to be rare and thus fail to explain the pervasiveness of the eMSTO feature. Furthermore, the age spread scenario cannot explain other CMD features that are consistent with a single stellar population (e.g. Li, de Grijs & Deng

---

★ E-mail: lorenzo.martinelli@uon.edu.au

2014a, b; Bastian & Niederhofer 2015; Wu et al. 2016; Li et al. 2016b). For instance, while the model explains some clusters with eRCs, it struggles with clusters with compact RCs (Li, de Grijs & Deng 2014b). Finally, clusters with eMSTOs often have a narrow sub-giant branch (SGB), inconsistent with a large internal age spread (Li et al. 2014a, 2016b; Bastian & Niederhofer 2015; Wu et al. 2016).

High-resolution spectroscopy of clusters with an eMSTO and eRC have revealed a systematic difference in the projected rotation velocities ($v \sin i$, where v is the surface velocity and i is the stellar inclination) between stars in the red and blue regions of the eMSTO (Kamann et al. 2018, 2020; Bastian et al. 2018; Marino et al. 2018a, b; Sun et al. 2019). This suggests that stellar rotation is a plausible cause of the effects leading to eMSTOs.

According to the stellar rotation scenario, the broadening of the MSTO is primarily driven by *gravity darkening* (von Zeipel 1924; Espinosa Lara & Rieutord 2011), where the equator of a rapidly rotating star appears darker and cooler than its poles due to the variation in surface gravity caused by the centrifugal acceleration across the star's surface. This effect has been directly observed in some B- and F-type stars using interferometric imaging (van Belle 2012). Consequently, the measured effective temperature, and thus the colour and magnitude of a star, depend on the rotation rate and the inclination angle of the rotation axis relative to the line of sight.

Bastian & de Mink (2009) were the first to demonstrate that rotation could, at least partially, account for the eMSTOs. Rotation causes hydrodynamical instabilities and large-scale plasma motions in radiative regions, which is thought to induce the mixing of stellar material and transport of angular momentum and chemical elements (Maeder & Meynet 2000; Maeder 2009). However, Girardi, Eggenberger & Miglio (2011) argued that rotational mixing and gravity darkening exert opposing influences on a cluster's CMD, rendering their combined effects insufficient to explain the eMSTO width. However, their analysis was constrained to rotational speeds not exceeding 70 per cent of the critical velocity and neglected the effect of the inclination angle. Subsequent investigations, incorporating stars with rotation rates approaching critical velocities and the effect of inclination angles (e.g. Brandt & Huang 2015; Cordoni et al. 2018, 2024; Gossage et al. 2019; Dresbach et al. 2023), have shown that in some cases a distribution of rotation rates alone can qualitatively reproduce the observed eMSTOs. Additionally, the stellar rotation scenario can explain why clusters with eMSTOs exhibit a narrow SGB (Li et al. 2014a, 2016a; Bastian & Niederhofer 2015; Wu et al. 2016): as the rotation rates of sub-giant stars would rapidly decrease, leading to a morphology of the CMD feature that remains consistent with a single stellar population, provided that rotation-induced mixing does not significantly affect the lifetime and luminosity distribution of rotating stars (see Section 2.1.7). This observation may offer an opportunity to constrain the extent of rotation-induced mixing in stars, which remains one of the major sources of uncertainty in modelling the effects of stellar rotation (Salaris & Cassisi 2017). In clusters hosting B-type main-sequence stars, a non-negligible fraction exhibit Balmer emission. These stars, referred to as Be stars, are thought to be surrounded by optically thin circumstellar discs formed by rapid stellar rotation, with the emission lines originating from the disc (Slettebak 1988; Porter & Rivinius 2003; McSwain & Gies 2005; Martayan, Baade & Fabregat 2008; Rivinius, Carciofi & Martayan 2013; Bastian et al. 2016; Milone et al. 2018). The fraction of Be stars varies with spectral type. Recent studies have also revealed a population of UV-dim stars in older clusters such as NGC 1783 (Martocchia et al. 2023), which show reduced ultraviolet (UV) flux compared to normal A/F-type stars. In younger clusters, many Be stars display a similar UV-dim characteristic, suggesting a connection between circumstellar discs and UV attenuation (Milone et al. 2023b; Li et al. 2024). Fast rotators may develop decretion discs in which dust condenses in the outer regions, and in clusters older than approximately 1 Gyr the stars are not hot enough to ionize the disc material, so the discs may be detectable only through absorption signatures (D'Antona et al. 2023; Kamann et al. 2023; He, Li & Li 2025).

In 1D stellar evolution codes stellar rotation is treated according to the shellular rotation approximation (Kippenhahn & Thomas 1970; Endal & Sofia 1976; Meynet & Maeder 1997). Within the shellular approximation the transport of angular momentum is treated in two different ways: using a simple diffusion equation (Endal & Sofia 1978; Pinsonneault et al. 1989; Heger, Langer & Woosley 2000) such as in codes like MESA (Paxton et al. 2011, 2013, 2015, 2018, 2019; Jermyn et al. 2023) and PARSEC (Nguyen et al. 2022), KEPLER (Weaver, Zimmerman & Woosley 1978), STERN (Heger et al. 2000), or using an advectodiffusive equation (Zahn 1992; Meynet & Maeder 1997; Maeder & Zahn 1998; Maeder 2009) that consider the advective nature of the meridional flows adopted by GENEC (Eggenberger et al. 2008), STAREVOL (Palacios et al. 2006; Decressin et al. 2009), CESTAM (Marques et al. 2013), and FRANEC (Chieffi & Limongi 2013). Different stellar evolutionary models can also differ in the derivation of the diffusion coefficients for the rotationally induced instabilities, often leading to significantly different efficiencies of these processes under the same initial stellar parameters (Nandal et al. 2024). MESA follows the formulation of Heger et al. (2000), using a highly simplified order-of-magnitude approach, whereas GENEC and PARSEC V2.0 adopt a more physical description that prioritize self-consistency (Chaboyer & Zahn 1992; Meynet & Maeder 1997; Talon & Zahn 1997; Maeder 2009).

Additionally, current rotating models fail to predict the evolution of the internal rotation profile as inferred from seismic constraints, indicating that additional angular momentum transport processes are required beyond those currently implemented in standard stellar evolution codes (e.g. Beck et al. 2012; Eggenberger, Montalbán & Miglio 2012; Aerts, Mathis & Rogers 2019; Eggenberger et al. 2019). This demonstrates that current rotating models are incomplete in their treatment of angular momentum transport, and highlights the need to constrain rotational mixing, whose effects are harder to isolate due to degeneracies with convective overshooting, composition, and age (Eggenberger, Lagarde & Charbonnel 2011).

The goal of this work is to test how different formulations of rotation-induced mixing, which predict significantly different mixing efficiencies, affect the CMD of intermediate-age synthetic star clusters with a distribution of initial stellar rotation rates. Using the MESA stellar evolution code, we compute two grids of stellar models adopting, respectively, the default diffusive formulation and an approximation of the advective-diffusive formulation as implemented in GENEC models from Georgy et al. (2013).

This paper is organized as follows. In Section 2, we describe the input physics of the stellar models, including the implementation of rotation and the prescriptions for rotation-induced mixing adopted in our grids. Section 3 outlines the method used to find the best-fitting synthetic clusters of observed star clusters. In Section 4, we examine the impact of rotational mixing on the CMD features of synthetic clusters and analyse and discuss the properties of the best-fitting models for NGC 419 and NGC 1817. Our conclusions are presented in Section 5.

Table 1. Summary of the adopted physics and characteristics of the stellar models in `grid 1` and `grid 2`.

Ingredient	Adopted prescriptions and parameters	Reference	Grid
Inital chemical composition (solar scaled)	$X_{\rm ini} = 0.7244$, $Y_{\rm ini} = 0.2611$, $Z_{\rm ini} = 0.0145$	Section 2.1.1	1 & 2
Equation of state	Default	Jermyn et al. (2023)	
Opacity	OPAL Type I for $\log T \geq 3.88$; Ferguson for $\log T < 3.88$; Type I → Type II at the end of H burning	Iglesias & Rogers (1993, 1996) Ferguson et al. (2005)	1 & 2 1 & 2
Nuclear reaction network	`pp_and_cno_extras.net` tracks 25 species: ^{1}H, ^{2}H, ^{3}He, ^{4}He, ^{7}Li, ^{7}Be, ^{8}B, ^{12}C, ^{13}C, ^{13}N, ^{14}N, ^{15}N, ^{14}O, ^{15}O, ^{16}O, ^{17}O, ^{18}O, ^{17}F, ^{18}F, ^{19}F, ^{18}Ne, ^{19}Ne, ^{20}Ne, ^{22}Mg, ^{24}Mg		1 & 2
Nuclear reaction rates	Default except for: ^{14}N(p, γ)^{15}O; ^{12}C(α, γ)^{16}O;	Jermyn et al. (2023) Imbriani et al. (2005) Kunz et al. (2002)	1 & 2
Boundary conditions	`Trampedach_solar`	Trampedach et al. (2014); Ball (2021)	1 & 2
Element diffusion	Default settings; turned off for vanishing convective envelopes, stable convective cores and post MS	Jermyn et al. (2023)	1 & 2
Rotation	0.0, 0.1, 0.3, 0.5, 0.6, 0.7, 0.8, 0.9, 0.95 $\omega_{\rm i}$	Section 2.1.5	1 & 2
Convection	`mlt_option = 'ML1'`, $\alpha_{\rm MLT} = 1.95$	Böhm-Vitense (1958)	1 & 2
Core overshoot	Exponential overshooting: $f = 0.0174$	Herwig (2000); Paxton et al. (2011)	1
	Step overshooting: $\alpha_{\rm ov} = 0.1$	Paxton et al. (2011); Georgy et al. (2013)	2
Envelope undershoot	Step undershooting: $\alpha_{\rm ov} = 0.2$	Paxton et al. (2011); Khan et al. (2018)	1
Rotational mixing	Diffusive implementation: $f_c = 1/30$, $f_\mu = 0.05$	Heger et al. (2000); Pinsonneault et al. (1989)	1
	custom	Appendix A	2
Mass loss	MS with rotational boost: $\eta_{\rm Dutch} = 1.0$, $\xi = 0.43$, boost factor capped at 10^4, implicit mass loss to keep $\Omega < \Omega_{\rm crit}$ RGB: none AGB: $\eta_{\rm Bloecker} = 0.2$	Glebbeek et al. (2009); Paxton et al. (2013) de Jager, Nieuwenhuijzen & van der Hucht (1988); Langer (1998) Bloecker (1995)	1 & 2

2 GRIDS OF STELLAR MODELS WITH ROTATION

In this section, we describe the physics included in the stellar evolutionary models and the implementation of stellar rotation. We use the publicly available, open-source, one-dimensional stellar evolution code, *Modules for Experiments in Stellar Astrophysics* (MESA; Paxton et al. 2011, 2013, 2015, 2018, 2019; Jermyn et al. 2023), version r-24.03.1. All models start from the pre-main sequence and extend up to the first few pulses of the thermally pulsating asymptotic giant branch. We compute two grids of models, that differ only in the implementation of rotation-induced mixing of chemical elements and convective core overshooting, referred to as `grid 1` and `grid 2`, and described in detail in Sections 2.1.4 and 2.1.7. The grids of stellar models span the mass range 0.6–4.0 $M_\odot$, with a step of 0.1 $M_\odot$ for $0.6 \leq M < 1.7$ $M_\odot$ and $3.0 < M \leq 4.0$ $M_\odot$, and a finer step of 0.025 $M_\odot$ for models with $1.7 \leq M \leq 3.0$ $M_\odot$. The finer mass resolution between 1.7 and 3.0 $M_\odot$ is crucial to resolve the transition from degenerate to non-degenerate core helium ignition, which is key to modelling the secondary clump and understanding the eRCs in intermediate-age clusters (Girardi et al. 1998; Girardi 1999; Girardi, Mermilliod & Carraro 2000).

2.1 Stellar evolutionary models

Here, we describe the different physics adopted in the stellar models of both `grid 1` and `grid 2`. The most relevant settings adopted in the stellar evolutionary models are summarized in Table 1, while the `inlist_project` and `run_star_extras.f90` files containing the complete settings are available on Zenodo: https://doi.org/10.5281/zenodo.15601753.

2.1.1 *Solar-scaled abundances*

The reference adopted for calculating the solar-scaled abundances is the solar chemical composition from Asplund et al. (2009). In this work, we adopted $\Delta Y/\Delta Z = 1.5$, a value consistent with that derived from the protosolar abundances of Asplund et al. (2009) and within the commonly accepted range (from about 1.4 to 2.5, see Serenelli & Basu 2010). A similar choice is made by Choi et al. (2016) and Ziółkowska et al. (2024).

We computed models for two different values of the metal mass fraction, $Z = 0.01$ and $Z = 0.004$, which approximately match the metallicities of the star clusters NGC 1817 and NGC 419, respectively (see Sections 4.1 and 4.2).

2.1.2 Microphysics

We used the default MESA equation of state described in Jermyn et al. (2023), the OPAL opacity tables (Iglesias & Rogers 1993, 1996) for $T \gtrsim 10^4$, and opacity tables from Ferguson et al. (2005) for $T \lesssim 10^4$.

We selected a nuclear reaction network named `pp_and_cno_extras.net`, that incorporates reactions from the pp chain and CNO cycle, as well as those associated with helium burning and the burning of heavier elements. We adopted nuclear reaction rates relevant for $T < 10^7$ K from the NACRE compilation (Angulo et al. 1999) across all temperatures. For the remaining reactions, we use rates from JINA REACLIB (Cyburt et al. 2010), or those from Caughlan & Fowler (1988) when not available in either NACRE or JINA REACLIB. Additionally, we updated the specific reaction rates for ^{14}N(p, γ)^{15}O from Imbriani et al. (2005) and ^{12}C(α, γ)^{16}O from Kunz et al. (2002).

We included atomic diffusion, neglecting radiative acceleration, and left most of the MESA controls relevant to atomic diffusion fixed to their default values. The implementation of atomic diffusion in MESA is described in Paxton et al. (2015, 2018). Since we neglected radiative acceleration, atomic diffusion was switched off, to avoid excessive helium and metal depletion in the outer layers, when either the mass fraction of the outer convective envelope fell below 0.5 per cent of the total stellar mass or the star developed a persistent convective core, consistent with the PARSEC models (Bressan et al. 2012).

2.1.3 Model atmosphere

To model the transition from the opaque depths to the observable outer layers and set the appropriate boundary conditions, we used the $T(\tau)$ relation from Ball (2021). This relation is an analytic fit to the radiation-coupled hydrodynamics simulations of near-surface convection with solar parameters by Trampedach et al. (2014) and is broadly representative of the full grid of simulations from the same work. This choice is implemented in MESA using the setting `atm_T_tau_relation = ''Trampedach_solar''`.

2.1.4 Convection and overshooting

Convective mixing in MESA is treated as a time-dependent diffusive process with a diffusion coefficient computed within the mixing length theory (MLT) formalism (Böhm-Vitense 1958). We fixed the free parameter of the MLT, $\alpha_{\rm MLT} = 1.95$, the initial metallicity $Z_{\rm ini} = 0.0145$, and the helium mass fraction $Y_{\rm ini} = 0.2611$ by calibrating a solar model. We determined the radial boundaries of convective regions using the Schwarzschild criterion except for the convective core boundary during core helium burning, which we treated according to the *moderate overshooting* (MOV) scheme described in section 2 of Bossini et al. (2017).

In `grid 1`, we used the exponential function for core overshooting prescribed in Herwig (2000) and Paxton et al. (2011), using $f_{\rm ov} = 0.0174$[1] for stars with $M > 1.1$ M$_\odot$. Below this mass limit, we did not apply any overshooting following the results of Claret & Torres (2017). However, we chose not to implement the gradual increase of the overshooting free parameter from 1.1 to 2 M$_\odot$, as suggested in the same study, in order to avoid imposing a predefined trend on core boundary mixing efficiency that could obscure the effects of rotation-induced mixing, and to remain consistent with the treatment adopted in `grid 2`.

In `grid 2`, we used the step overshooting prescription (Paxton et al. 2011). For stars with $M > 1.1$ M$_\odot$ we adopted an $\alpha_{\rm ov} = 0.1$ to be consistent with the choice in the grid of GENEC models in Georgy et al. (2013), which served as our reference grid for calibrating the efficiency of rotation-induced mixing. As in `grid 1`, we did not include overshooting for stars $M \le 1.1$ M$_\odot$. This lower amount of overshooting in `grid 2` is compensated by the significantly larger efficiency of rotational mixing in the convective boundary region as in the rotating models of Georgy et al. (2013).

In both `grid 1` and `grid 2`, we set the convective core overshoot during the core helium burning phase with a step overshooting with $\alpha_{\rm ov} = 0.5$ as in Bossini et al. (2017). Below the convective envelope, we implemented an exponential overshooting with $f = 0.02$ following Khan et al. (2018).

2.1.5 Rotation

We initialized all rotating models to have solid body rotation at a fraction of the critical velocity $\omega_{\rm i} = \Omega_{\rm i}/\Omega_{\rm crit}$ just before the zero age main sequence (ZAMS). The effects of rotation on the stellar structure equations are included in MESA using the *shellular approximation* (Kippenhahn & Thomas 1970; Endal & Sofia 1976; Meynet & Maeder 1997; Heger et al. 2000; Paxton et al. 2013, 2019), for which MESA solves the stellar structure equations in one dimension by projecting them along the isobars, with shape determined by the Roche potential (Maeder 2009; Paxton et al. 2019). MESA employs analytical fits to the Roche potential of a point mass, enabling the calculation of the structure of rotating stars up to $\omega \approx 0.9$ (Paxton et al. 2019).

Different definitions of the critical rotational velocity (Rivinius et al. 2013) are used in various stellar evolution codes. MESA adopts the following definition (Paxton et al. 2013):

$$\Omega^2_{\rm crit,MESA} = \left(1 - \frac{L}{L_{\rm Edd}}\right)\frac{GM}{R^3}, \tag{1}$$

where L is the total luminosity, M is the total mass, G is the universal gravitational constant, R is the total radius, neglecting deviations from spherical symmetry, and $L_{\rm Edd} = 4\pi cGM/\kappa$ is calculated as a mass-weighted average in a user-specified optical depth range (with the default value $\tau \in [1\text{–}100]$). Here, c is the speed of light, and κ is the Rosseland mean opacity. For $L/L_{\rm Edd} \sim 0$, as in our case, the critical angular and linear velocities are then defined as

$$\Omega_{\rm crit,MESA} = \sqrt{\frac{GM}{R_e^3}} \quad \text{and} \quad \upsilon_{\rm crit,MESA} = \sqrt{\frac{GM}{R_e}}, \tag{2}$$

where $\upsilon_{\rm crit,MESA}$ is the orbital velocity at the equator, $\Omega_{\rm crit,MESA}$ is the corresponding angular velocity, and R_e is the equatorial radius of the rotating star. A more physically motivated definition in the context of this study is the critical velocity in the Roche model (Maeder 2009)

$$\Omega_{\rm crit} = \sqrt{\frac{GM}{R^3_{\rm e,crit}}} = \sqrt{\frac{8}{27}\frac{GM}{R^3_{\rm p,crit}}}. \tag{3}$$

In this framework, the critical linear velocity at the equator is defined as

$$\upsilon_{\rm crit} = \sqrt{\frac{GM}{R_{\rm e,crit}}} = \sqrt{\frac{2}{3}\frac{GM}{R_{\rm p,crit}}}, \tag{4}$$

---

[1] This value corresponds to $\alpha_{\rm ov} \approx 0.2$ in the step overshooting prescription (Claret & Torres 2017).

noting that in this case $\Omega/\Omega_{\rm crit} \neq v/v_{\rm crit}$. Here, $R_{\rm e,crit}$ and $R_{\rm p,crit}$ are the equatorial and polar radii of a critically rotating star, respectively.[2] For more details, see Maeder (2009). This definition is widely used in studies of stellar rotation statistics (Royer, Zorec & Gómez 2007) and is adopted by several stellar evolution codes, such as GENEC (Eggenberger et al. 2008) and PARSEC (Nguyen et al. 2022).

For stellar models with identical input physics, mass, chemical composition, and initial ω, but with different definitions of the critical velocity, the model using equation (1) exhibits equatorial velocities, $v_{\rm eq}$, approximately 1.6 times larger than using equation (3). Following Wang et al. (2023), we convert $W := \Omega/\Omega_{\rm crit,MESA}$ to $\omega := \Omega/\Omega_{\rm crit}$, and vice versa, using equation (11) in Rivinius et al. (2013) and its inverse

$$\omega = \left(\frac{3W^{2/3}}{2+W^2}\right)^{3/2}. \tag{5}$$

Note that $W = \omega$ only for non-rotating and critically rotating stars.

To account for the latitudinal variation of surface temperature and flux, we adopt the gravity darkening model of Espinosa Lara & Rieutord (2011), which applies at any rotation rate and agrees well with interferometric observations of fast rotators (Espinosa Lara & Rieutord 2011; Belle 2012). The luminosity measured by an observer at inclination i with respect to the rotation axis is

$$L_{\rm MES}(i) = 4\pi \int_{\boldsymbol{d\Sigma}\cdot\boldsymbol{d}>0} I(\theta)\,\boldsymbol{d\Sigma}\cdot\boldsymbol{d}, \tag{6}$$

where $I(\theta)$ is the specific intensity at colatitude θ, integrated over the visible hemisphere. Assuming blackbody radiation, this becomes:

$$L_{\rm MES}(i) = 4\sigma \int_{\boldsymbol{d\Sigma}\cdot\boldsymbol{d}>0} T_{\rm eff}^4(\theta)\,\boldsymbol{d\Sigma}\cdot\boldsymbol{d}. \tag{7}$$

The corresponding effective temperature inferred by the observer is

$$T_{\rm eff,MES} = \left(\frac{L_{\rm MES}}{\sigma\Sigma_p}\right)^{1/4}, \tag{8}$$

where Σ_p is the projected surface area perpendicular to the line of sight, and σ is the Stefan–Boltzmann constant. This expression differs from the standard definition of the effective temperature,

$$T_{\rm eff} = \left(\frac{L}{\sigma\Sigma}\right)^{1/4}, \tag{9}$$

where Σ is the total surface area of the star.

Another important aspect of rotation, particularly for stars with masses below approximately 1.5 $\mathrm{M}_\odot$, is magnetic braking (Kraft 1967). Low-mass dwarfs rapidly lose their initial angular momentum due to magnetized stellar winds, a process that is both theoretically expected and observed in the distribution of rotational velocities in star clusters and field stars (Beyer & White 2024). However, rotation and magnetic activity are related to stellar age, mass, and metallicity through a complex relationship that remains not fully understood. With precise stellar ages from asteroseismology, the relationship between age, rotation, mass, and magnetic activity requires a 'weakened magnetic braking' to explain the observations (e.g. van Saders et al. 2016; Metcalfe et al. 2020). In the absence of a detailed magnetic braking model, we adopt a simplified approach to approximate its effects. Below a certain mass threshold, that depends on metallicity, we force models to be non-rotating. We limit the maximum $\omega_{\rm i}$ (see Section 2.1.5 for definition) that the stars can have for each stellar mass between $M_{\rm norot}$ and $M_{\rm rot}$, and this maximum increases with mass from $M_{\rm norot}$ to $M_{\rm rot}$ where the full range of rotation rates is computed. For example, for models with $Z = 0.01$ we set $M_{\rm norot} = 1.3$ $\mathrm{M}_\odot$ and $M_{\rm rot} = 1.6$ $\mathrm{M}_\odot$; and for models with $Z = 0.004$, we use $M_{\rm norot} = 1.2$ $\mathrm{M}_\odot$ and $M_{\rm rot} = 1.5$ $\mathrm{M}_\odot$. The decrease of $M_{\rm norot}$ and $M_{\rm rot}$ with metallicity is included to roughly account for the findings of Amard & Matt (2020), which show that metal-poor stars experience less efficient spin-down at ages $\gtrsim$1 Gyr. A similar approach is employed in Gossage et al. (2019) to mimic magnetic braking in low-mass stars in synthetic star clusters.

2.1.6 Mass loss

For slow rotators in the range of masses we covered, a negligible amount of mass-loss occurs throughout the MS. For a fast rotator however, it is possible to reach the critical rotation velocity during the MS, even if it started on the ZAMS with $\omega_{\rm i} < 1$. Once critical rotation is attained, the effective gravity at the equator of the star vanishes. We therefore expect a strong enhancement of the mass-loss in the equatorial region, which removes overcritical layers and maintains the surface at, or slightly below, critical rotation velocity. A description of this specific process is not yet included in stellar evolution codes, and numerically it is not yet possible to maintain the model at the critical velocity. To overcome this, we used a radiative wind prescription based on Jager et al. (1988) with a rotationally enhanced mass-loss (as in Paxton et al. 2013). Rotationally enhanced mass-loss is adjusted iteratively before the next time-step until the rotation rate at the surface is slightly sub-critical ($\omega_{\rm max} = 0.99$). In effect, this is an implicit solution for the mass-loss (of the order of 0.1 per cent of the total mass for the models with $\omega_{\rm i} = 0.9$ and a much smaller fraction for slower rotators) when rotation is close to becoming supercritical (Paxton et al. 2013).

For the age range we considered (0.8–1.5 Gyr), asteroseismic measurements of mass for stars in open clusters suggests very little or null red giant branch (RGB) mass-loss (e.g. Handberg et al. 2017). Therefore we did not include mass-loss on the RGB in our models, but did include mass-loss with $\eta_B = 0.2$ for the asymptotic giant branch (Bloecker 1995).

2.1.7 Rotation induced transport of angular momentum and chemical elements

In line with most available stellar model grids including rotation, we consider only hydrodynamical transport processes for angular momentum and chemical elements (Georgy et al. 2013; Choi et al. 2016; Nguyen et al. 2022). In `grid 1`, we adopted the default MESA fully diffusive formulation of rotation-induced mixing, as described in Heger et al. (2000). This formulation considers five rotationally induced hydrodynamical instabilities: dynamical shear instability, secular shear instability, Solberg–Høiland instability, Eddington–Sweet circulation, and Goldreich–Schubert–Fricke instability. There are two free parameters in this implementation: f_c, a number between 0 and 1 that represents the ratio of the diffusion coefficient to the turbulent viscosity; and f_μ, that encodes the sensitivity of rotational mixing to the mean molecular weight gradient, ∇_μ (Heger et al. 2000; Paxton et al. 2013). We chose $f_c = 1/30$ and $f_\mu = 0.05$ following Pinsonneault et al. (1989) and Heger et al. (2000).

In `grid 2`, we adopted a custom rotational mixing prescription during the MS, calibrated to emulate the transport of chemical

---

[2] The variation of the polar radius R_p due to rotation is small, so $R_{\rm p,crit}/R_p \approx 1$ is a reasonable approximation (Ekström et al. 2008). Therefore, equations (4) and (3) can be calculated without requiring a numerical model of a critically rotating star.

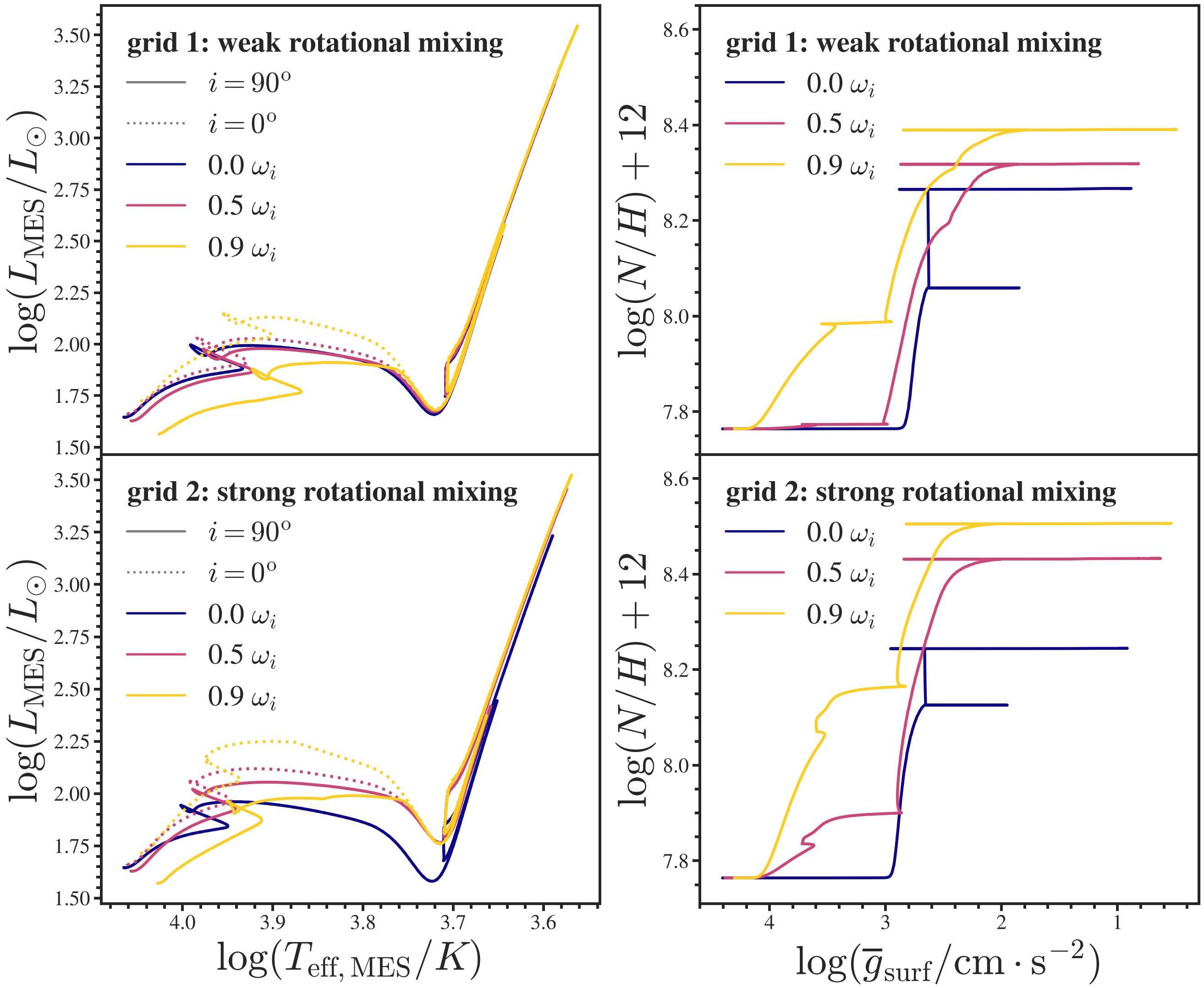

Figure 1. Left: Evolutionary tracks of 2.5 $M_\odot$ models at $Z = 0.01$ with initial rotation rates 0.0, 0.5, and 0.9 $\omega_{\rm i}$, viewed at an inclination angle $i = 90^{\rm o}$ (solid) and $i = 0^{\rm o}$ (dotted), for `grid 1` (top) and `grid 2` (bottom). The evolutionary track without rotation in `grid 1` exhibit a more extended main sequence than that in `grid 2`, due to the larger convective core overshooting adopted in `grid 1` (see Section 2.1.4). Gravity darkening on the evolutionary tracks presented in this figure is calculated in a manner consistent with Espinosa Lara & Rieutord (2011). Right: Evolution of the surface nitrogen-to-hydrogen ratio as a function of the average surface gravity for the same models with `grid 1` models in the top panel and `grid 2` models in the bottom panel.

elements and the evolution of surface equatorial velocity in the GENEC models of Georgy et al. (2013). The calibration of the diffusion coefficients for this prescription is described in Appendix A. GENEC adopts an advective-diffusive approach that includes the effects of meridional circulation and shear instabilities. The diffusion coefficients are derived within a self-consistent framework, under certain assumptions, and require the calibration of a single free parameter (Eggenberger et al. 2008; Maeder 2009; Georgy et al. 2013). In the post-main sequence, we switch to the default MESA mixing.[3] This approach for `grid 2` allowed us to approximate the rotation-induced mixing of chemical elements from GENEC models within MESA (see Appendix A), removing discrepancies due to differing input physics and assumptions between codes, and isolating differences in internal mixing efficiency between the two model grids. Importantly, this hybrid method enabled the computation of the helium-burning phase in stars with masses below 2.5 $M_\odot$, outside of the GENEC computational regime. Furthermore, we extended `grid 2` to masses below the 1.7 $M_\odot$ limit of Georgy et al. (2014), by linearly extrapolating the calibrated diffusion coefficients (as described in Appendix A) to match the mass limits with `grid 1`, but we must refrain from drawing conclusions in this mass range when using `grid 2`.

At the start of the MS, rotational effects are nearly identical in both grids (see left panel of Fig. 1), with rotating models seen equator-on ($i = 90^\circ$) showing lower measured luminosities and effective temperatures due to gravity darkening. For pole-on views ($i = 0^\circ$), the measured luminosity increases moderately, and the effective temperature shifts slightly towards higher values. However, as the star evolves on the main sequence, differences in the efficiency of rotational mixing become increasingly significant. In `grid 2`, rotational mixing more efficiently supplies fresh hydrogen fuel to

---

[3] Note that GENEC models also switch to a fully diffusive transport of angular momentum and chemical elements in the post-MS phases (Nandal et al. 2024).

the core and transports helium and other H-burning products into the radiative zone. By increasing the size of the convective core and altering the chemical composition profiles in the radiative zone, rotational mixing induces an increase in luminosity and a widening of the main sequence (discussed in detail in Eggenberger et al. 2011). The models of `grid 1` (top right panel of Fig. 1) exhibit a significantly smaller change in the nitrogen-to-hydrogen ratio compared to the models of `grid 2` (bottom).

`grid 1` and `grid 2` represent two commonly used approaches for implementing rotation-induced mixing in stellar models. The first is adopted in grids like `MIST` (Choi et al. 2016; Gossage et al. 2019), the second in GENEC (Georgy et al. 2013). We attempt, for the first time, to constrain the impact of these different prescriptions using observations of intermediate-age star clusters with rotationally extended MSTOs.

3 SYNTHETIC CLUSTERS

We computed synthetic clusters and isochrones from `grid 1` and `grid 2` by interpolating the evolutionary tracks using the SYCLIST code (see Georgy et al. 2014, for details). We describe our method, which follows the *equivalent evolutionary points* (EEPs) approach described in Dotter (2016) closely, and compare the resulting isochrones with those from other data bases in Appendix B.

We created a basis of single age synthetic stellar populations each with a uniform distribution of ω_i in a $\Delta\omega_i = 0.1$ bin, centred at $\omega_i = 0.05, 0.15, 0.25, 0.35, 0.45, 0.55, 0.65, 0.75, 0.85, 0.95$. Each *base stellar population* (BSP) contains 1.5×10^5 stars with mass between 0.6 and 4.0 $\mathrm{M}_\odot$ adopting a Salpeter (1954) initial mass function. BSPs were computed with ages ranging from $\log(\mathrm{age/yr}) = 8.900$ to $\log(\mathrm{age/yr}) = 9.180$, spaced by 0.005 dex in age. We assumed a uniformly distributed orientation of the rotation axis which corresponds to a $\sin i$ probability distribution for the viewing angle i. Gravity and limb darkening were treated following Espinosa Lara & Rieutord (2011) and Howarth (2011), respectively. For implementation details, see Georgy et al. (2014). BSPs were computed adopting a binary fraction of 0.2, roughly consistent with the binary fractions found for NGC 419 (Rubele et al. 2010) and NGC 1817 (de Juan Ovelar et al. 2019) star clusters. The members of binary systems were drawn from the same grids of single stellar models and treated as unresolved binaries in the synthetic CMD as in Hurley & Tout (1998).

We found the best-fitting synthetic clusters for both NGC 419 (Section 4.1) and NGC 1817 (Section 4.2) by searching the optimal age and combination of BSPs that best reproduce the distribution of stars on the eMSTO and eRC of these clusters. As demonstrated in Section 4, these two features are the most sensitive to the effects of rotation, rotational mixing, and age. Moreover, the field contamination for these CMD features is negligible in both the studied clusters (Girardi et al. 2009; Sandquist et al. 2020).We defined a parallelogram encompassing the eMSTO (see Figs 2 and 3), with its long axis aligned along the direction in which gravity darkening extends the MSTO. This direction is determined by connecting the reddest and bluest points of two isochrones with $\omega_\mathrm{i} = 0.9$, viewed equator-on and pole-on, respectively. For this preliminary step, the isochrone ages and metallicities were adopted from previous literature estimates for each cluster (Sandquist et al. 2020; Ettorre et al. 2025). The size of the eMSTO parallelogram was chosen to enclose both the observed eMSTO and the MSTOs of all BSPs across the full age grid. We excluded the Kraft break region from this selection, since our models do not include a reliable treatment of magnetic braking and its inclusion could bias the fitting procedure. A second parallelogram was defined to encompass the eRC (see Figs 2

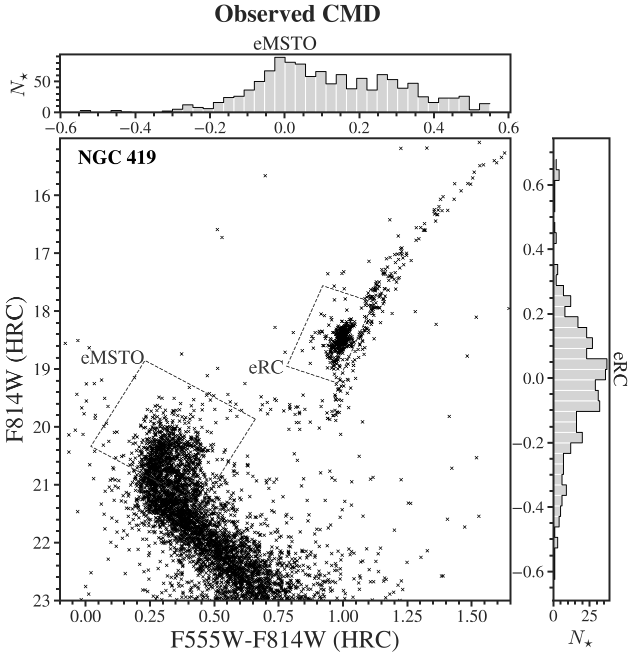

Figure 2. Observed CMD of NGC 419 from the HST programme GO-10396 (PI: J. S. Gallagher), specifically the ACS/HRC data were reduced by Girardi et al. (2009). The dashed parallelograms are the eMSTO and eRC regions described in Section 3. The top panel represents the histogram of star counts projected along the long axis of the eMSTO parallelogram, while the right panel represents the histogram of star counts projected along the long axis of the eRC parallelogram.

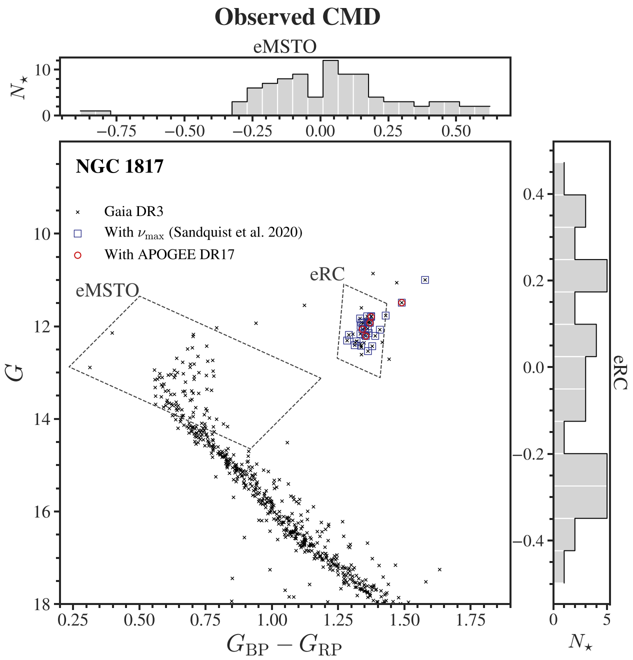

Figure 3. Observed CMD of NGC 1817. The stars enclosed in boxes have ν_max measured by Sandquist et al. (2020) from K2 data. The stars enclosed in circles have also APOGEE DR17 spectroscopic parameters (Willett et al. submitted). The dashed parallelograms and the top and right panels are defined in the same way as Fig. 2.

and 3), with its long axis aligned with the observed extension of the eRC. This direction was determined by connecting the brightest and faintest points of the eRC. The size of the eRC parallelogram was set to best isolate the observed eRC from the RGB and early-AGB (asymptotic giant branch), while still enclosing the RC of all BSPs across the age grid. We projected the coordinates of the stars within the eMSTO and eRC parallelograms along their respective long axes and constructed histograms of star counts for both the observations and the synthetic clusters (top and right panels of Figs 2 and 3). The best-fitting synthetic cluster was identified by determining the optimal combination of BSPs and age that minimizes the sum of the negative logarithmic Poisson likelihood ratios of the eMSTO and eRC histograms

$$-\ln\mathcal{L}_\mathrm{P} = \sum_{i=\mathrm{eMSTO}}^{\mathrm{eRC}} \sum_{k=1}^{N_\mathrm{bins}} m_k^i - n_k^i + n_k^i \ln\frac{n_k^i}{m_k^i}, \qquad (10)$$

where k indexes the histogram bins in each region i. This statistic is particularly suited to our analysis since it properly accounts for the discrete and Poissonian nature of star counts (Dolphin 2002; Cordoni et al. 2022; Ettorre et al. 2025).

The different BSPs are multiplied by a scaling factor, C_j, which specifies the contribution of each BSP to the final synthetic cluster before being combined. The coefficients C_j can take values between 0 and 1. To minimize $-\ln\mathcal{L}_\mathrm{P}$ and determine the optimal set of C_j and the cluster age, we employed the genetic algorithm implemented in the PYGAD PYTHON library (Fawzy Gad 2021), which reduces the risk of converging to a local minimum and facilitates the search for the global solution.

4 THE IMPACT OF ROTATIONAL MIXING ON EXTENDED MAIN-SEQUENCE TURN-OFFS AND EXTENDED RED CLUMPS

A selection of BSPs centred at different rotation rates and ages, for both `grid 1` (weak rotational mixing) and `grid 2` (strong rotational mixing), is shown in Fig. 4. These BSPs have been transformed into the observational plane of NGC 419 as described in Section 4.1. For visualization purposes, we display only a random sub-sample of 10^4 stars from the original BSPs.

The top panels of Fig. 4 show three BSPs from `grid 1`. For reference, the dashed and dotted red lines mark the eRC magnitude of peak density and the average SGB magnitude of NGC 419, respectively. From top left to top right: the first two correspond to the same age of ∼1.10 Gyr [log(age/yr) = 9.040] but are centred at different rotation rates, $\omega_i = 0.55$ and $\omega_i = 0.85$, respectively; the third BSP corresponds to an age of ∼1.26 Gyr [log(age/yr) = 9.100] and is centred at $\omega_i = 0.85$. Four clear effects emerge as the average ω_i and age increases:

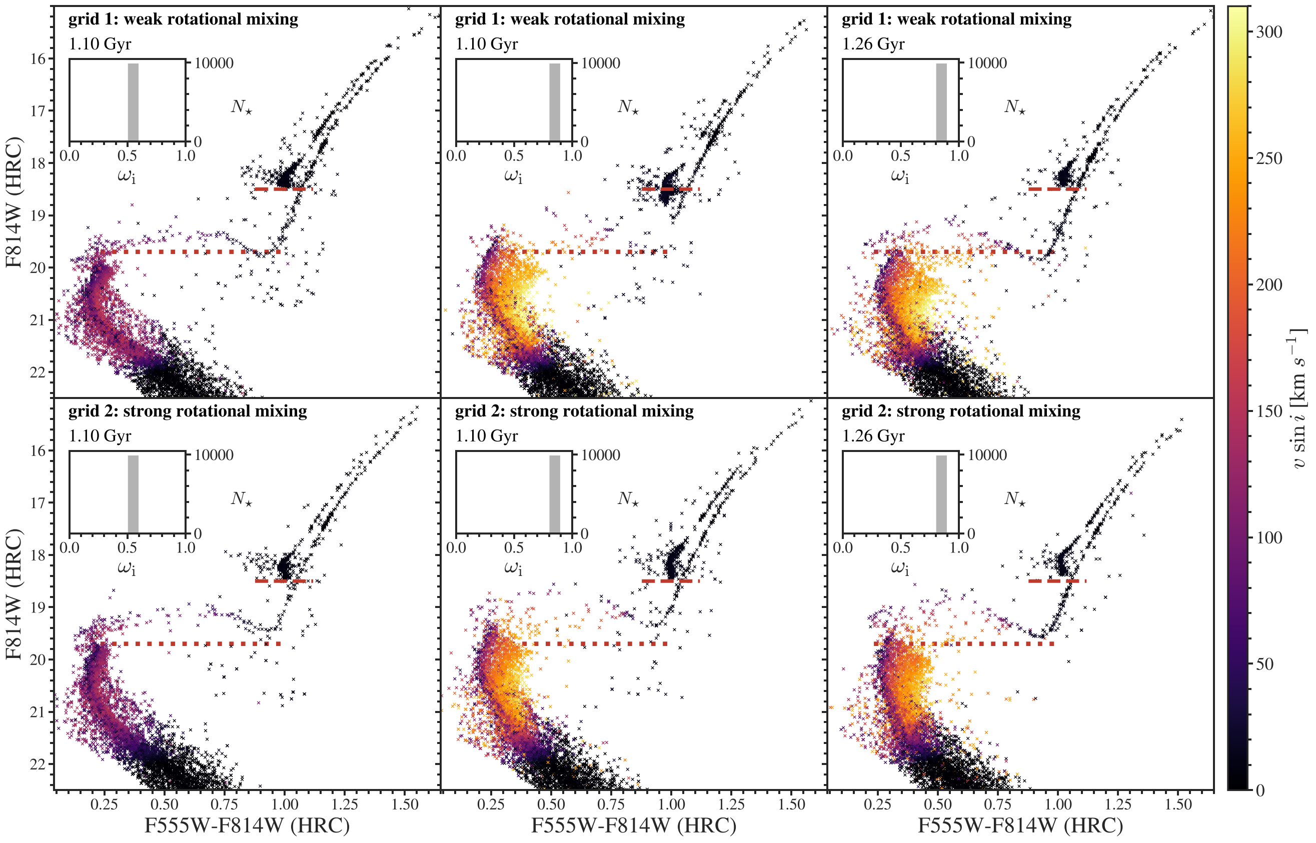

Figure 4. CMDs of selected BSPs at different rotation rates and different ages, for both `grid 1` (top panels) and `grid 2` (bottom panels), transformed into the observational plane of NGC 419 as described in Section 4.1. Going from left to right, for both the top and bottom panels, the following BSPs are represented: ∼ 1.10 Gyr [log(age/yr) = 9.040] centred at $\omega_i = 0.55$, ∼ 1.10 Gyr centred at $\omega_i = 0.85$, ∼ 1.26 Gyr (log(age/yr) = 9.100) centred at $\omega_i = 0.85$. The colour map represents the projected rotational velocity $v \sin i$ of the stars. For representation purposes we selected only a random sub-sample of 10^4 stars from the original BSPs. The inset histogram shows the distribution of initial rotation rates ω_i of the stars in the BSP. For reference, the dashed and dotted red lines mark the eRC magnitude of peak density and the average SGB magnitude of NGC 419, respectively.

(i) Gravity darkening broadens the MSTO region: stars observed at $i \sim 90^\circ$ (large $v \sin i$) appear redder and fainter, while those at $i \sim 0^\circ$ (small $v \sin i$) appear slightly bluer and brighter.

(ii) Gravity darkening also widens the early portion of the SGB, which then narrows towards the base of the RGB as stellar rotation decreases with envelope expansion.

(iii) At an age of ∼1.10 Gyr, rotational mixing extends the RC to fainter magnitudes and slightly bluer colours. This effect arises from rotational mixing triggered by fast rotation during the MS phase, rather than from the stars' current rotational velocities. In the case of the eRC of NGC 419, Dresbach et al. (2023) argued that the slow rotation of RC stars rules out significant rotational effects, but this interpretation overlooks the role of rotational mixing during the MS. With an average $\omega_i = 0.55$, only the compact primary RC, populated by stars that ignited helium in fully degenerate cores and experienced the He flash, is present. In contrast, with an average $\omega_i = 0.85$, both the primary and secondary clumps appear. Even the weak rotational mixing of `grid 1` models at ∼1.10 Gyr is sufficient to slightly increase the He-core mass, allowing the initially fastest rotators to avoid the He flash by reaching helium ignition before the core becomes fully degenerate, thus populating the secondary clump.

(iv) At an age of ∼1.26 Gyr and an average $\omega_i = 0.85$, (i) and (ii) remain valid as in the ∼1.10 Gyr case, whereas (iii) no longer applies. At this older age, rotational mixing is no longer sufficient to increase the He-core mass beyond the threshold required to avoid helium ignition in fully degenerate cores, so all stars undergo the He flash and end up in the compact primary RC. This naturally explains the case of clusters that display an eMSTO but a compact RC (e.g. Li et al. 2014a, b, 2016b, 2024).

It is interesting to note that only the case with an eRC, at an age of ∼1.10 Gyr and centred at $\omega_i = 0.85$, matches the magnitude of peak density of the eRC in NGC 419 (red dashed line in Fig. 4). This is consistent with the interpretation of the NGC 419 eRC as a combination of primary and secondary RC populations (Girardi et al. 2009).

The bottom panels of Fig. 4 show three BSPs corresponding to those in the top panels but computed from `grid 2` models. Considerations (i), (ii), (iii), and (iv) made for `grid 1` still apply, but with three key differences:

(i) With an average $\omega_i = 0.85$, the post-MS phases appear ∼0.5 mag brighter and slightly bluer than in the case of weak rotational mixing from `grid 1`. This is a consequence of the strong rotational mixing in `grid 2` models, which transports helium and other H-burning products into the radiative zone and significantly increases the size of the convective core. The resulting higher mean molecular weight in the envelope and larger He-core mass lead to brighter post-MS phases (Maeder 2009; Eggenberger et al. 2011; Salaris & Cassisi 2017).

(ii) For the same average ω_i, the eMSTO is less extended compared to the case of `grid 1`. This results from the strong rotational mixing in `grid 2` models, which counteracts the effect of gravity darkening. While gravity darkening shifts stars observed nearly equator-on towards redder colours and fainter magnitudes, rotational mixing tends to move stars towards bluer colours and brighter magnitudes, regardless of their inclination to the line of sight (Girardi et al. 2011).

(iii) For the same average ω_i, the maximum $v \sin i$ of eMSTO stars is lower in the `grid 2` case.

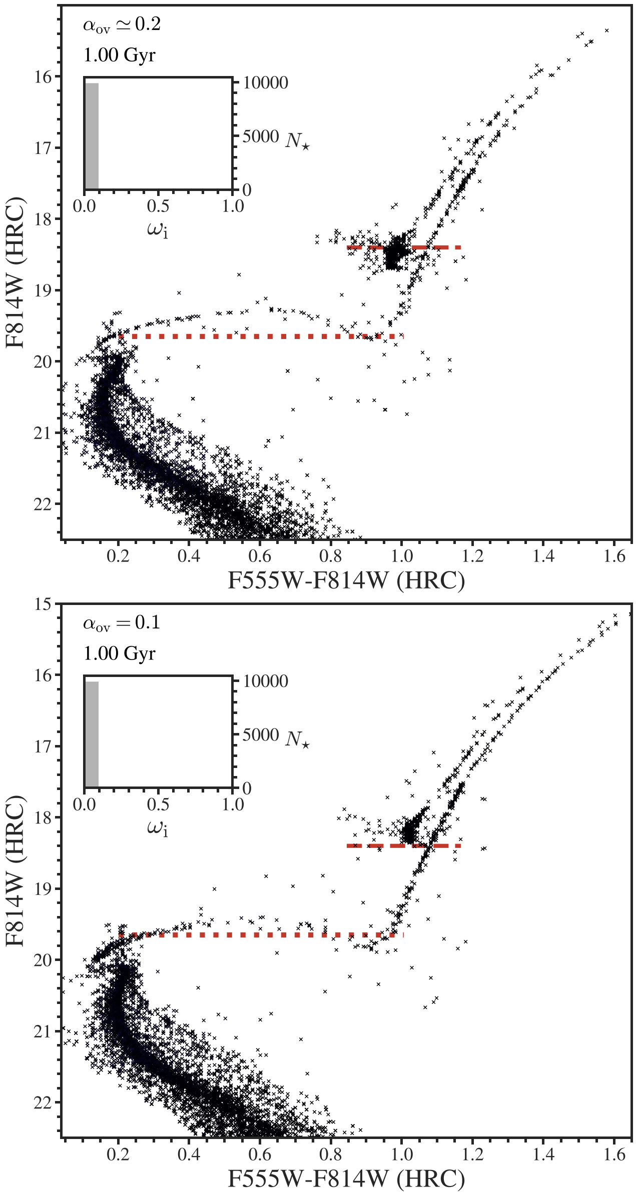

Figure 5. CMDs of two BSPs with an age of 1 Gyr centred at $\omega_i = 0.05$ (inset histogram) with different amount of convective core overshooting: $\alpha_{\rm ov} \simeq 0.2$ (top panel) and $\alpha_{\rm ov} = 0.1$ (bottom panel) transformed into the observational plane of NGC 419 as described in Section 4.1. For representation purposes we selected only a random sub-sample of 10^4 stars from the original BSPs. For reference, the dashed and dotted lines mark the eRC magnitude of peak density and the average SGB magnitude of NGC 419, respectively.

It is interesting to note that none of the BSPs computed with `grid 2` models match the magnitude of peak density of the eRC (red dashed line in Fig. 4) or the average magnitude of the SGB (red dotted line in Fig. 4) of NGC 419.

It must be acknowledged that the amount of convective core overshooting during the MS can affect, in a way similar (though not identical) to rotational mixing, the magnitudes of the post-MS phases (Eggenberger et al. 2010) and influence whether a cluster exhibits an eRC or a compact RC at a given age. Fig. 5 shows two BSPs with a central $\omega_i = 0.05$ (essentially non-rotating) at an age of 1.0 Gyr, but with different amounts of convective core overshooting. At this age, the BSP with larger overshooting (top panel of Fig. 5) exhibits an eRC with both primary and secondary clump and a slightly brighter SGB, whereas the BSP with smaller overshooting (bottom panel of Fig. 5) displays a compact RC (primary RC only) and a slightly fainter SGB.

We selected two representative star clusters for modelling: the Small Magellanic Cloud (SMC) cluster NGC 419 and the Milky Way open cluster NGC 1817. Both clusters exhibit prominent eMSTOs and eRCs (Girardi et al. 2009; Sandquist et al. 2020) and are known to host fast-rotating stars on the MSTO. In Sections 4.1 and 4.2, we present the best-fitting synthetic clusters for NGC 419 and NGC 1817, constructed using stellar models from `grid 1` and `grid 2`, as described in Section 3.

4.1 NGC 419

NGC419 is an intermediate-age (~ 1.26 Gyr; Ettorre et al. 2025) globular cluster in the SMC, exhibiting one of the most extended eMSTOs and an eRC observed to date. This cluster is believed to host a secondary clump of helium-burning stars that are just massive enough to avoid full electron degeneracy in their hydrogen-exhausted cores, alongside slightly less massive stars that ignited helium in a degenerate core (Girardi et al. 2009). Additionally, Kamann et al. (2018) found a range of $v \sin i$ values between the blue and red MSTO stars in this cluster (see Section 4.1.1).

We used the observations of NGC 419 from the *HST* programme GO-10396 (PI: J. S. Gallagher), specifically the Advanced Camera for Surveys High Resolution Channel (ACS/HRC) data were reduced by Girardi et al. (2009). We adopted a metallicity of $Z = 0.004$, consistent with the value $[\mathrm{Fe/H}] = -0.58 \pm 0.02$ dex derived for NGC 419 by Mucciarelli et al. (2023). Synthetic photometry was transformed into the observational plane using the `YBC` bolometric corrections (Chen et al. 2019), which include variable extinction coefficients for the *HST* ACS/HRC $F814W$ and $F555W$ filters. We adopted the distance modulus $(m - M)_0 = 18.85 \pm 0.03$ mag from Goudfrooij et al. (2014) and a colour excess $E(B - V) = 0.061^{+0.026}_{-0.033}$ mag from the reddening map by Skowron et al. (2021). We applied to the synthetic CMDs the photometric errors and incompleteness derived from artificial star tests performed on the original HRC images.

By simultaneously fitting the distributions of stars in the eMSTO and eRC (Section 3), we obtained for `grid 1` a best-fitting age of $1.11^{-0.03}_{+0.05}$ Gyr, characterized by a dominant population of fast rotators ($\omega_i \gtrsim 0.75$) and a smaller contribution from slower rotators ($\omega_i \simeq 0.55$; see inset in Fig. 6a). A similarly high fraction of fast rotators in NGC 419 is also found in the best-fitting model of Ettorre et al. (2025), although their derived age (~ 1.26 Gyr) is significantly older. This difference in best-fitting age arises primarily from the different fitting approach, as they varied metallicity, distance, and foreground extinction while fitting the full CMD, whereas we fixed these parameters based on independent observations and focused on the eMSTO and eRC. In addition, differences in the adopted physics of the PARSEC V2.0 models (Nguyen et al. 2022), including the implementation of rotational mixing as well as the mass and rotation rate resolution of the grids, which differ from both our `grid 1` and `grid 2`, likely contribute to the discrepancy in the derived ages.

For `grid 2` we found a best-fitting age of $0.97^{-0.03}_{+0.05}$ Gyr, a high fraction of fast rotators with $\omega_i \gtrsim 0.85$ and a much smaller contribution of slower rotators with $\omega_i \simeq 0.4$ (see inset in Fig. 6b). The uncertainties were computed by repeating the optimization through 1000 Monte Carlo realizations, varying $E(B - V)$, $(m - M)_0$ within the uncertainties and bootstrapping with replacement the observed CMD of NGC 419. We neglected the contribution of the 0.02 dex uncertainty in [Fe/H], as it produces negligible perturbations in the CMD compared to the uncertainties in $E(B - V)$ and $(m - M)_0$.

The best-fitting synthetic cluster found using `grid 1` (weak rotational mixing) gives a $-\ln \mathcal{L}_\mathrm{P} = 233.90$, which is significantly smaller than that found for `grid 2` (strong rotational mixing case) that gives a $-\ln \mathcal{L}_\mathrm{P} = 627.51$.

The inability to achieve a best-fitting with `grid 2` comparable to that obtained with `grid 1` is due to the much stronger rotational mixing. As discussed in Section 4, in `grid 2` the strong rotational mixing systematically increases the brightness and slightly shifts all CMD features towards bluer colours, starting from the eMSTO. In addition, it slightly reduces the width of the eMSTO.

It is worth noting that the `grid 2` best-fitting synthetic cluster is significantly younger than the `grid 1` best fit. Although an older age would better reproduce the eMSTO, a younger age provides a better match to the faint extension of the eRC. This trend is also seen with `grid 1`, but in the case of `grid 2` the RC brightness is so strongly increased by rotational mixing that no satisfactory compromise can be achieved.

The best-fitting synthetic cluster obtained with `grid 1`, although significantly better than that from `grid 2`, still shows discrepancies that suggest some ingredients in our rotating models are either poorly modelled or missing. The eMSTO in the best-fitting cluster contains an excess of stars on the bright blue side, where pole-on fast rotators are expected. Even with a large fraction of near-critical rotators ($\omega_i \simeq 0.95$), the faint red side of the eMSTO remains slightly less extended than observed. Similar limitations have been reported in other studies (Goudfrooij, Girardi & Correnti 2017; Gossage et al. 2019; Lipatov, Brandt & Gossage 2022), where rotation alone could not reproduce the full eMSTO extension without invoking ad hoc assumptions on the orientation distribution of rapid rotators.

The SGB of the best-fitting cluster is also on average slightly brighter than observed. While the eRC is broadly well reproduced in both magnitude and colour, it does not extend to magnitudes as faint as in the observation.

4.1.1 *Rotation across the eMSTO of NGC 419*

For NGC 419, Kamann et al. (2018) derived average $v \sin i$ values of 87 ± 16 and 130 ± 22 km s^{-1} for stars in two regions spanning the blue and red MSTO, respectively. These values were obtained from combined spectra of stars selected within boxes that contain roughly equal numbers of stars on either side of the eMSTO. Fig. 7 shows the distribution of $v \sin i$ across the CMD for our best-fitting synthetic cluster of NGC 419 from `grid 1` (left panel of Fig. 6). The projected rotational velocities exhibit a clear trend, with lower values on the bluer side of the eMSTO and higher values on the redder side. This trend closely resembles the $v \sin i$ distribution observed across the eMSTO of NGC 1846 by Kamann et al. (2020). Applying the same box definitions as Kamann et al. (2018) to our synthetic CMD, we computed average $v \sin i$ values of 170 ± 68 and 258 ± 62 km s^{-1} for the blue and red MSTO regions, respectively.

In our synthetic cluster, the projected rotational velocities are systematically higher than the observed values of Kamann et al. (2018), with a larger difference between the blue and red MSTO regions.

This systematically larger $v \sin i$ in the synthetic clusters is also found by Bastian et al. (2018) and Kamann et al. (2020, 2023). It is interesting to note that the possibility of stars in the synthetic cluster rotating too rapidly is consistent with the overabundance on

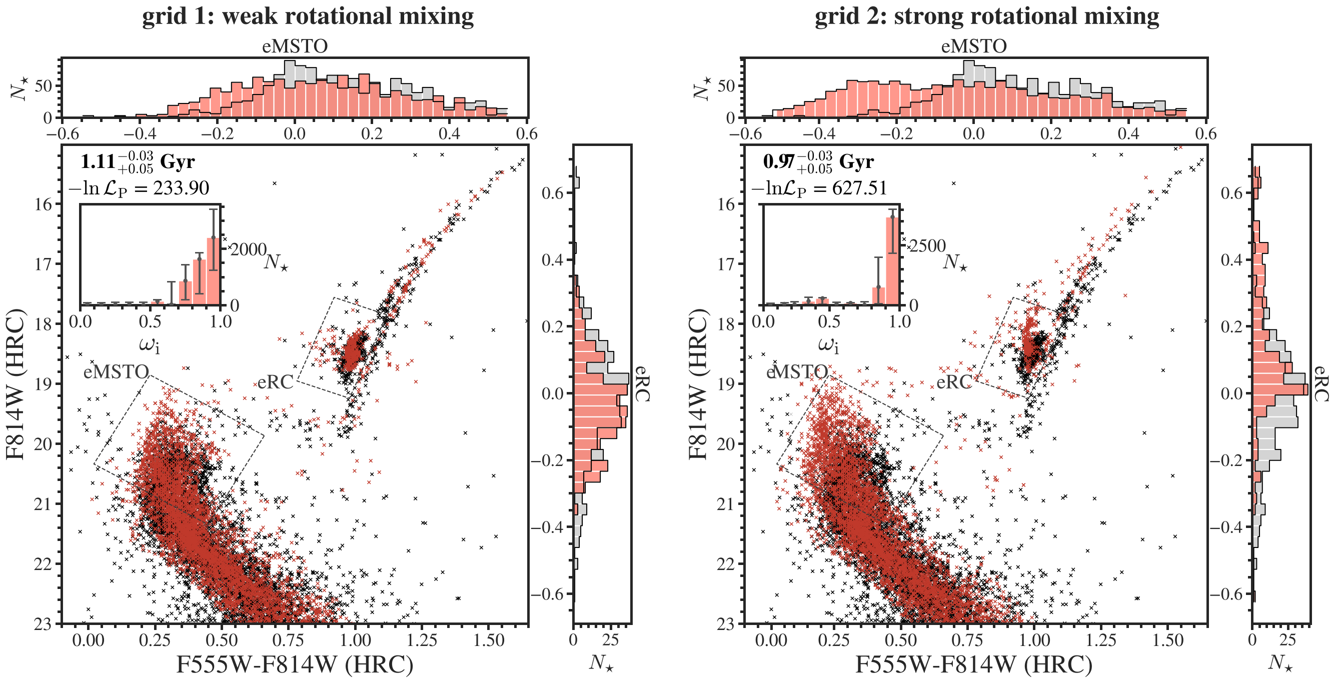

(a) (b)

Figure 6. Left: Best-fitting CMD (red) obtained combining BSPs from `grid 1` stellar models (weak rotational mixing) and the observed CMD of NGC 419 (black). Right: Best-fitting CMD (red) obtained combining BSPs from `grid 2` stellar models (strong rotational mixing) and observed CMD of NGC 419 (black). Each panel includes an inset with the distribution of initial stellar rotation rates ω_i for the corresponding synthetic cluster, along with the age of the best-fitting synthetic cluster and the value of the negative logarithmic Poisson likelihood ratio $-\ln\mathcal{L}_\mathrm{P}$. The dashed parallelograms are the regions described in Section 3 to study the distribution of stars across the eMSTO and eRC, respectively. The histograms in the top and right panels show the star counts projected along the long axis of the eMSTO and eRC parallelograms, respectively. The best-fitting synthetic cluster is shown in red, and the observations of NGC 419 are shown in black.

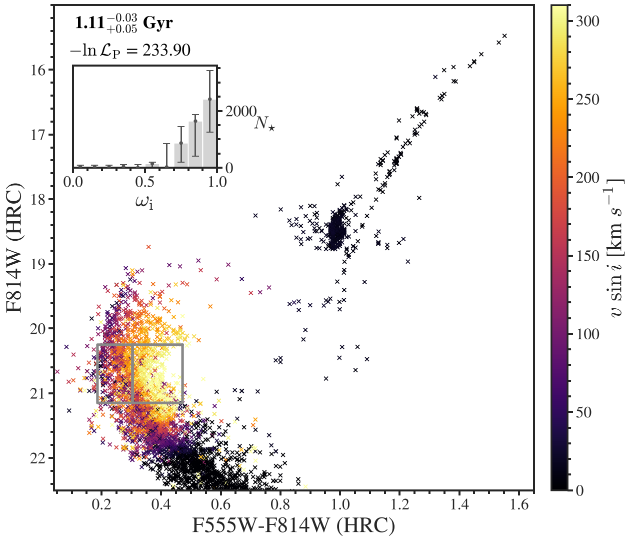

Figure 7. CMD of our best-fitting synthetic cluster for NGC 419 from `grid 1` stellar models (left panel of Fig. 6), coloured by $v \sin i$. The inset shows the histogram of initial rotation rates for the stars in the best-fitting synthetic cluster. The grey boxes replicate the regions of the eMSTO where Kamann et al. (2018) measure the average $v\ \sin i$ of NGC 419 stars. We obtained average $v \sin i$ values of 170 ± 68 and 258 ± 62 km s^{-1} for the blue and red MSTO regions, respectively.

the bright blue side of our best-fitting synthetic cluster (Fig. 6a), where pole-on fast rotators tend to be located. The magnitude of this discrepancy, however, should be interpreted with caution, as measurement for almost critically rotating stars can be biased towards lower values because of the rotationally induced darkening of the equatorial regions of the star (Townsend, Owocki & Howarth 2004). Kamann et al. (2018) also note that systematic uncertainties in their MUSE measurements, due to the instrument's relatively low spectral resolution, could reach up to 30 km s^{-1}. Additionally any inaccuracy in the modelling of gravity darkening and bolometric corrections not specifically calibrated for rapidly rotating stars (Girardi et al. 2019) could alter the best-fitting distribution of initial rotation rates required to reproduce the eMSTO morphology and, consequently, the predicted $v \sin i$ values across it.

An intriguing hypothesis is closely related to the phenomenon of Be (Bastian et al. 2016; Milone et al. 2018) and UV-dim stars (Martocchia et al. 2023; Milone et al. 2023b). It is possible that a large fraction of the fast rotators in these clusters develop decretion discs when they reach high rotation rates, and that dust grains condense in the outer regions of these discs (D'Antona et al. 2023; He et al. 2025). In clusters with ages around 1.0 Gyr or older, such discs may not be easily identifiable in emission, unlike for Be stars in younger clusters, since they are not hot enough to ionize the disc material. These stars could instead be identified in absorption (Kamann et al. 2023). The red side of the eMSTO could then be populated by moderately fast rotating stars whose dust rings intercept the line of sight, causing extinction of stellar light. The reddest UV-dim stars may represent

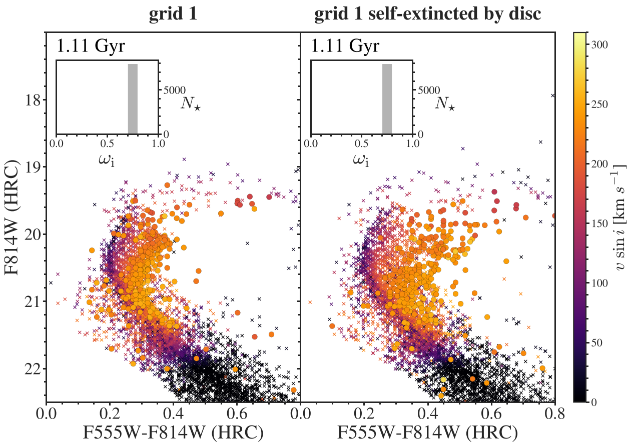

Figure 8. Right: CMD of a ∼1.11 Gyr (log(age/yr) = 9.045) old BSP from `grid 1` models centred at $\omega_i = 0.75$ (inset histogram) and coloured by $v \sin i$. Left: CMD of the same BSP but including the contribution of the simple model of self-extinction by the decretion disc in stars observed within the disc opening angle and rotating faster than $v/v_\mathrm{crit} \gtrsim 0.7$ described in Section 4.1.1.

the extreme tail of the distribution, corresponding to both maximum obscuration and orientations where the dust ring is aligned with the line of sight. When only gravity darkening is considered, the eMSTO extension can be reproduced only by extremely fast rotators ($\omega_i > 0.9$) observed close to equator-on. This would imply very high projected rotational velocities ($v \sin i \gtrsim 300$ km s^{-1}) that are not observed.

Instead, observations indicate that Be stars typically rotate at an average of $v/v_\mathrm{crit} \sim 0.7$ (Rivinius et al. 2013; Dufton et al. 2022; Kamann et al. 2023). If decretion discs can form at sub-critical rotation, through mechanisms that facilitate mass ejection such as the pulsationally driven orbital mass-ejection model (Kee et al. 2016), then stars rotating at lower v/v_crit could still be subject to extinction caused by the disc when viewed within the disc opening angle. In this case, the additional extinction may be sufficient to account for the observed width of the eMSTO without invoking extremely rapid rotators.

We tested this idea with a simple experiment. Lacking a complete model of the disc structure and its wavelength- and angle-dependent optical depth, we explored the effect of increasing the reddening $E(B-V)$ for stars in our synthetic cluster rotating at $v/v_\mathrm{crit} \gtrsim 0.7$ and observed within ∼15° of the equatorial plane. We modulate the reddening with a Gaussian dependence on the viewing angle i, and scale it with a logistic function of the normalized equatorial velocity

$$E(B-V) \rightarrow E(B-V)\left[1 + 2 \cdot \mathcal{G}(i)\mathcal{S}(v_\mathrm{eq}/v_\mathrm{crit})\right], \tag{11}$$

where $\mathcal{G}(i)$ is a Gaussian with $\sigma_i = 15^\circ$ (Kamann et al. 2023) centred at $\mu_i = 90^\circ$, and

$$\mathcal{S}(x) = 1/\left[1 + \exp\left(-\frac{x-0.7}{0.08}\right)\right] \tag{12}$$

is a logistic factor that increases sharply for stars rotating faster than ∼70 per cent of the critical velocity, and saturates such that the total reddening reaches up to three times the interstellar value. In absolute terms, this corresponds to a maximum additional extinction of $E(B-V) = 0.122$ mag from the disc. Fig. 8 shows the CMD of a BSP at ∼1.11 Gyr (log(age/yr) = 9.045) with central $\omega_i = 0.75$, transformed into the observational plane as described in Section 4.1. The maximum $v \sin i$ across the eMSTO is consistent with observations of intermediate-age clusters (Bastian et al. 2018; Kamann et al. 2020), but it is significantly lower than in our best-fitting synthetic cluster (Fig. 7). Nevertheless, the MSTO remains relatively narrow. The right panel of Fig. 8 shows the same CMD after applying the reddening scaling of equation (11) to account for self-extinction by the decretion disc in stars observed within the disc opening angle and rotating faster than $v/v_\mathrm{crit} \gtrsim 0.7$. The effect broadens the eMSTO while maintaining realistic $v \sin i$ values and avoiding overpopulation of the blue-bright region by fast, pole-on rotators, unlike in our best-fitting synthetic cluster (Figs 6a and 7). We emphasize that this experiment is highly schematic: the amount of extinction produced by the disc, its dependence on rotation, and the use of the interstellar extinction curve may not accurately reflect the true properties of disc-generated extinction. Decretion-disc formation could alter the stars' angular momentum evolution and internal transport processes, including rotational mixing. This experiment therefore provides a zeroth-order test of the concept, demonstrating its potential and motivating further investigation. A detailed modelling of the disc structure and extinction curve is required and lies beyond the scope of this work. If physical models of decretion discs, including their optical depths, indicate a comparable impact in terms of self-extinction, this could significantly influence the inferred rotation distributions, cluster ages, and constraints on rotational mixing in clusters exhibiting an eMSTO.

4.2 NGC 1817

NGC 1817 is a massive intermediate-age Galactic open cluster, approximately 1 Gyr old (Cordoni et al. 2018; Sandquist et al. 2020), that exhibits a clear eMSTO and eRC. Sandquist et al. (2020) suggest the presence of a subset of stars in the core helium-burning (CHeB) phase with core masses near the minimum required for non-degenerate helium ignition (i.e. secondary clump stars), along with more massive clump stars that have not yet evolved off the RC.

Sandquist et al. (2020) also show that it is not possible to simultaneously reproduce the eMSTO and eRC using a single non-rotating isochrone. Analysing the eMSTO, Cordoni et al. (2018) propose that stellar rotation, particularly the presence of stars rotating near critical velocity, may account for the observed morphology. This interpretation is consistent with the observation of Molenda-Żakowicz et al. (2009), who measured a range of $v \sin i$ values across the MSTO (see Section 4.2.2).

Cluster members were identified by Hunt & Reffert (2024) using the *Gaia* DR3 catalogue (Gaia Collaboration 2023). Their photometry was then corrected for differential reddening following the procedure of Milone et al. (2009) and adapted to open clusters by Cordoni et al. (2018). First, we used the *Gaia* G_BP and G_RP reddening coefficients from Casagrande & VandenBerg (2018) to define the reddening direction and rotate the G_RP versus $G_\mathrm{BP} - G_\mathrm{RP}$ CMD, aligning the reddening vector with the new x-axis. Next, we determined the fiducial line of the rotated CMD from a sample of reference stars, defined as bright main-sequence stars, excluding clear unresolved binary stars. Finally, we computed the distance, along the x-axis, of each reference star from the fiducial line. To calculate the differential reddening associated with each cluster star, we selected the 25 neighbouring reference stars and calculated the median distance along the reddening line. We excluded each reference star from the determination of its own differential reddening. The corresponding error is calculated as the root mean scatter of the distance values divided by $\sqrt{N-1}$.

This cluster was observed during Campaign 13 of the *K2* mission, and Sandquist et al. (2020) measured average asteroseismic parameters (ν_max and/or $\Delta\nu$) describing solar-like oscillation spectra of 29

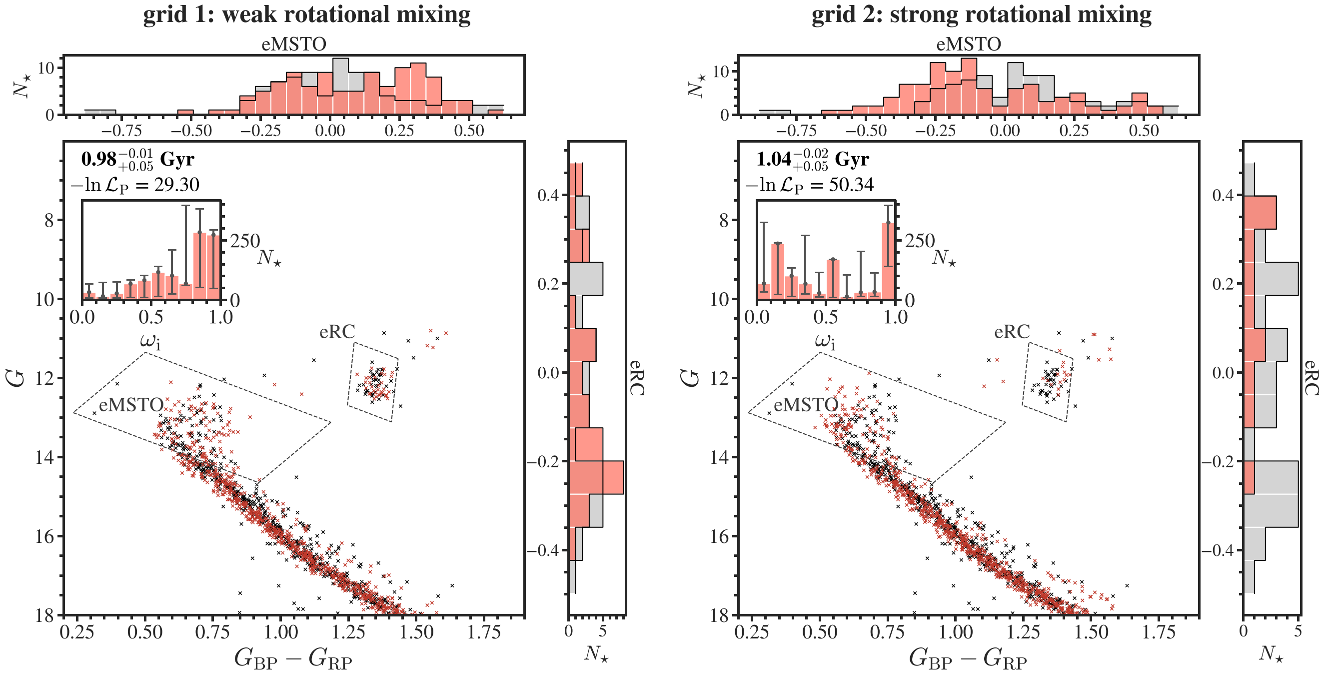

(a)

(b)

Figure 9. Left: Best-fitting CMD (red) obtained combining BSPs from `grid 1` stellar models (weak rotational mixing) and the observed CMD of NGC 1817 (black). Right: Best-fitting CMD (red) obtained combining BSPs from `grid 2` stellar models (strong rotational mixing) and observed CMD of NGC 1817 (black). The figure structure is identical to that of Fig. 6.

giants, most of which were identified as RC stars. For five of these giants, spectroscopic chemical abundances and stellar parameters are available in the Willett et al. (submitted) catalogue, based on the *Apache Point Observatory Galactic Evolution Experiment* (APOGEE) *Data Release 17* (DR17) spectra (Majewski et al. 2017; Abdurro'uf et al. 2022).

For modelling NGC 1817 we adopted a metallicity of $Z = 0.010$, consistent with the values $[\mathrm{Fe/H}] = -0.08 \pm 0.02$ and $[\mathrm{Fe/H}] = -0.11 \pm 0.03$ derived for NGC 1817 by Casamiquela et al. (2017). Synthetic photometry was transformed into the observational plane using the `YBC` bolometric corrections (Chen et al. 2019), which account for variable extinction coefficients in the *Gaia* DR3 G, G_BP, and G_RP bands. The distance modulus used to shift the synthetic cluster magnitudes was derived from the median *Gaia* DR3 parallax of NGC 1817 stars. A zero-point correction was applied following Lindegren et al. (2021), using the relevant parameters from the *Gaia* DR3 archive. This yielded a distance modulus of $(m - M)_0 = 11.101 \pm 0.008$. To estimate the colour excess $E(B - V)$, we used five NGC 1817 giants with spectroscopic T_eff and $\log g$ from *APOGEE* DR17 spectra (Willett et al. submitted), and determined the value that best matched their *Gaia* DR3 $G_\mathrm{BP} - G_\mathrm{RP}$ colours using the `YBC` bolometric corrections. This procedure yielded $E(B - V) = 0.228 \pm 0.008$.

By simultaneously fitting the distributions of stars in the eMSTO and eRC (Section 3), for `grid 1` we found a best-fitting age of $0.98^{-0.01}_{+0.05}$ Gyr, characterized by a dominant fraction of fast rotators ($\omega_i \gtrsim 0.85$) and a smaller contribution from slower rotators (see inset in Fig. 9a). For `grid 2` we found a best-fitting age of $1.04^{-0.02}_{+0.05}$ Gyr, a high fraction of fast rotators with $\omega_i \sim 0.95$ and a moderate contribution of slower rotators (see inset in Fig. 9b). The uncertainties were computed following the same procedure described in Section 4.1. The best-fitting synthetic cluster found using `grid 1` (weak rotational mixing) gives a $-\ln \mathcal{L}_\mathrm{P} = 29.30$, which is smaller than that found for `grid 2` (strong rotational mixing case) that gives a $-\ln \mathcal{L}_\mathrm{P} = 50.34$.

In the case of NGC 1817, the much smaller number of stars limits the statistical significance, and caution is required. However, for the eMSTO and eRC, where the number of stars is sufficient to allow some general conclusions, the results appear similar to those obtained for NGC 419. The best-fitting synthetic cluster based on `grid 1` provides a good match to the eMSTO and eRC magnitudes, colours, and widths. The best-fitting synthetic cluster obtained with `grid 2` yields a clearly worse fit, showing the same issues seen for NGC 419: a significant overabundance of stars on the bright blue side of the eMSTO, a lack of stars on the faint red side, and an eRC that is on average brighter than observed. No conclusions can be drawn for the SGB and RGB, as these phases are too sparsely populated in this cluster.

Despite the limitations posed by the small number statistics in this cluster, the results still allow us to rule out strong rotational mixing, as implemented in the `grid 2` models. Not only does it produce the same type of discrepancies between the synthetic clusters and the observations as in the case of NGC419, but these discrepancies are also consistent with the expected effects of rotational mixing discussed in Section 4 and illustrated in Fig. 4.

4.2.1 *Mass–luminosity diagram of red clump stars*

For NGC 1817, we also take advantage of the available asteroseismic parameter ν_max, derived from *K2* photometry for 29 giants by Sandquist et al. (2020), in combination with *Gaia* DR3 colours, magnitudes, and parallaxes, to test the predictions for the RC stellar

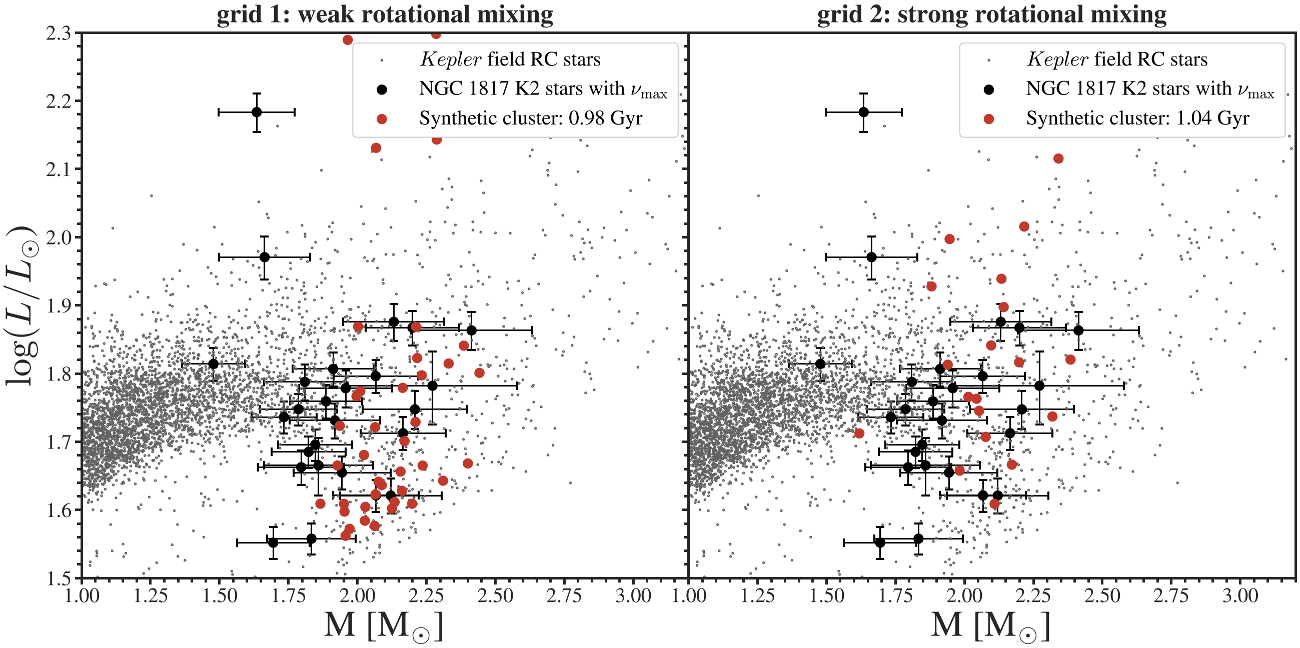

Figure 10. Mass–luminosity diagram of NGC 1817 giants with measured $\nu_{\max}$ from *K2* data (Sandquist et al. 2020) (black dots) and *Kepler* field RC stars from the catalogue of Willett et al. () (grey circles), shown in both panels. Red dots indicate the best-fitting synthetic cluster stars with $\nu_{\max} < 300\ \mu$Hz, from `grid 1` in the left panel and from `grid 2` in the right panel.

mass range and luminosity in synthetic clusters generated from rotating stellar models.

Sandquist et al. (2020) derived the masses and radii of these giants using the global asteroseismic parameters $\nu_{\max}$ and $\Delta\nu$, combined with photometric $T_{\rm eff}$ values inferred from $(b-y)$ colours, applying two standard scaling relations. However, due to the large uncertainties associated with $\nu_{\max}$ and $\Delta\nu$ measured from *K2* photometry, the resulting uncertainties on stellar mass were too large to provide useful constraints.

To overcome this, we derived stellar masses using the following asteroseismic scaling relation:

$$\frac{M_{\rm seis}}{{\rm M}_\odot} \simeq \left(\frac{\nu_{\max}}{\nu_{\max,\odot}}\right)\left(\frac{L}{L_\odot}\right)\left(\frac{T_{\rm eff}}{T_{\rm eff,\odot}}\right)^{-7/2}, \tag{13}$$

(e.g. Miglio et al. 2012), where luminosities and effective temperatures were computed from *Gaia* DR3 colours, magnitudes, and parallaxes corrected for the zero point offset following Lindegren et al. (2021). This relation, which uses only $\nu_{\max}$ as the asteroseismic input and relies on precise luminosities derived from *Gaia* DR3 photometry and parallaxes, allowed us to significantly reduce the uncertainties on the resulting asteroseismic masses (see Fig. 10).

Because the scaling relation in equation (13) depends only on global stellar properties, it avoids potential complications related to variations in helium core masses induced by different levels of rotational mixing. Knowledge of the intrinsic mass and luminosity of RC stars provides an additional constraint on internal mixing processes in earlier evolutionary phases, particularly during the main sequence.

The synthetic cluster masses, luminosities, and effective temperatures were derived in a manner consistent with the NGC 1817 data, starting from *Gaia* DR3 colours, magnitudes, and $\nu_{\max}$, with the input parameters perturbed according to the observational uncertainties before applying equation (13).

The stellar masses and luminosities in the eRC of the best-fitting synthetic cluster to NGC1817 computed with `grid 1` are consistent with the values obtained from observations (left panel of Fig. 10), highlighting the robustness of the model. This agreement further supports the good match observed in the CMD. In particular, the distribution of masses and luminosities closely follows that of *Kepler* field RC stars (grey dots in Fig. 10) around ~ 2.0 M$_\odot$, the mass corresponding to the minimum luminosity of He-burning stars and the transition between degenerate and non-degenerate He ignition (Girardi 1999). By contrast, the masses derived for NGC 1817 (using $\nu_{\max}$ measurements from *K2* data) appear to be systematically shifted to slightly lower values compared to the bulk of the *Kepler* field RC stars distribution around the transition mass. For the best-fitting synthetic cluster based on `grid 2`, the mass range of RC stars is also consistent with that obtained from observations, while the luminosity distribution is only partly consistent and extend to higher values than observed. However, the combination of small-number statistics and mass uncertainties does not allow us to significantly prefer one model over the other in the mass–luminosity diagram.

4.2.2 *Rotation across the eMSTO of NGC 1817*

Molenda-Żakowicz et al. (2009) measured $v \sin i$ values ranging from 45 to 225 km s^{-1} for 11 δSct variables located across the MSTO of NGC 1817. We cross-matched these stars with our *Gaia* DR3 catalogue of cluster members using TOPCAT (Taylor 2005), finding 10 matches. All of these, except for the star labelled V12 in Molenda-Żakowicz et al. (2009), were included in our list of cluster members. These 10 δ Sct variables are shown in Fig. 11, plotted on top of the our best-fitting synthetic cluster and colour-coded by their $v \sin i$ values using the same colour scale as for the synthetic cluster. Although the sample size is small and does not allow for statistically significant conclusions, the observed $v \sin i$ distribution

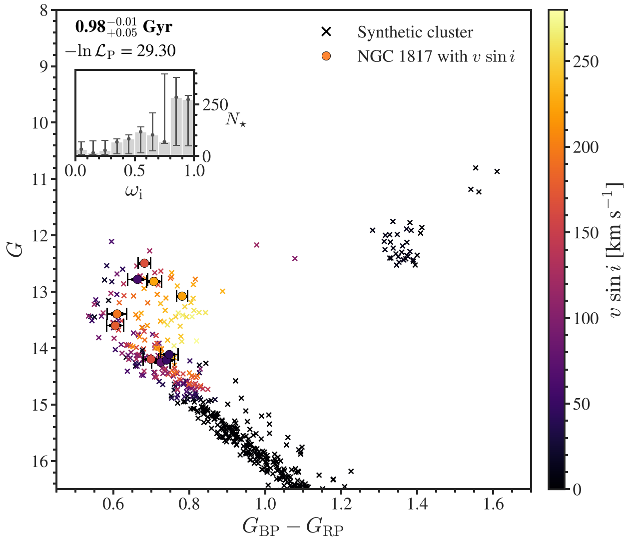

Figure 11. CMD of our best-fitting synthetic cluster for NGC 1817 from `grid 1` stellar models (left panel of Fig. 9). Synthetic stars are shown as crosses and coloured by their $v \sin i$ values. Overlaid are the 10 stars with $v \sin i$ measurements from Molenda-Żakowicz et al. (2009) (filled circles), using the same colour scale. The inset shows the histogram of initial rotation rates for the stars in the best-fitting synthetic cluster.

across the eMSTO appears consistent with the scenario seen in NGC 419, where stars on the blue side have lower $v \sin i$ and stars on the red side higher values, including the fact that the largest $v \sin i$ values predicted by the synthetic cluster for the red side tend to exceed the measured values in the same CMD region. Similar considerations as those discussed for the comparison between measured and synthetic $v \sin i$ in NGC 419 also apply here.

5 CONCLUSIONS

We have constructed two homogeneous grids of rotating stellar models with high resolution in both initial mass and rotation rate (see Section 2). These grids were computed using identical input physics, differing only in the treatment of convective core overshooting and the implementation of rotational mixing. One grid adopts the standard MESA prescription for rotation-induced mixing (`grid 1`), while the other is calibrated to reproduce the efficiency of rotational mixing in the GENEC models of Georgy et al. (2013) (`grid 2`). Both prescriptions are widely used in stellar models grids applied to studies of eMSTOs and stellar rotation. Stellar models from `grid 1` exhibit very limited effects of rotational mixing compared to those from `grid 2` (see Section 2.1.7 and Fig. 1).

We used these grids to generate a set of statistically independent single-age synthetic stellar populations, referred to as 'Base Stellar Populations', covering the full range of initial rotation rates from non-rotating to near-critical.

By analysing the CMDs and $v \sin i$ distributions of these BSPs across different ages, rotation rates, and convective core overshooting efficiencies, we assessed the relative roles of rotational mixing, gravity darkening, overshooting, and age in shaping eMSTOs and eRCs (see Section 4 and Fig. 4). This framework provides a natural explanation for the presence of both eMSTOs and eRCs in single-age populations, as well as for clusters that display eMSTOs but compact RCs.

We used an optimization algorithm to determine, the best combination of BSPs to fit the CMDs of two star clusters: the SMC cluster NGC 419 and the Milky Way open cluster NGC 1817, both of which display prominent eMSTOs and eRCs, and are known to host fast-rotating stars on the eMSTO (see Sections 4.1 and 4.2). For NGC 1817, we also obtained a precise estimate of the colour excess $E(B-V)$ from five red giant stars, using spectroscopic $T_{\rm eff}$ and $\log g$ from APOGEE DR17, combined with *Gaia* DR3 $G_{\rm BP} - G_{\rm RP}$ colour index. We further derived the most precise estimates to date of the RC star masses in this cluster, by combining $\nu_{\rm max}$ measurements from Sandquist et al. (2020) with luminosities and $T_{\rm eff}$ values derived from *Gaia* DR3 photometry and parallaxes. Our analysis of NGC 419 and NGC 1817 shows that the best-fitting synthetic clusters are obtained with models that include weak rotational mixing rather than strong mixing (see Figs 6 and 9), and that they require a high fraction of fast rotators with $\omega_i \gtrsim 0.85$, close to critical rotation. A similarly high fraction of fast rotators in NGC 419 and in other intermediate-age clusters has also been found by Ettorre et al. (2025).

NGC 419 and NGC 1817, while similar in age and both exhibiting eMSTO and eRC features, differ in important respects: they reside in distinct environments, the SMC and the Milky Way respectively, have different metallicities, and were observed independently with different instruments and processed through separate data reduction pipelines. Despite these differences, both clusters consistently indicate that strong rotational mixing, which would significantly modify the envelope composition, is disfavoured because it produces changes in luminosity and temperature that lead to worse CMD fits. Our results are further supported by the mass and luminosity range of RC stars derived for NGC 1817 (Fig. 10). It is not excluded, however, that rotational mixing could slightly increase the He-core mass at hydrogen exhaustion, potentially enough to affect the transition from degenerate to non-degenerate helium ignition (see Section 4 and Fig. 4).

A similar result was found by Brogaard et al. (2023) for the core He-burning stars in the open cluster NGC 6866, who concluded that the actual effects of rotation are smaller than those predicted by 1D GENEC models, which overestimate stellar radii compared to values derived from asteroseismology. It remains to be verified whether the same scenario is consistently supported by surface chemical abundance measurements of stars in these clusters.

The best-fitting synthetic clusters with weak rotational mixing are broadly consistent with the observations, but certain aspects, including systematically higher $v \sin i$ values on the red side of the eMSTOs, show discrepancies (Sections 4.1.1 and 4.2.2). Similar discrepancies have been identified in other studies (Bastian et al. 2018; Kamann et al. 2020, 2023). In some cases, even stars rotating near the critical limit fail to reproduce the full observed width of the eMSTO, suggesting that additional mechanisms may be required (Goudfrooij et al. 2017; Gossage et al. 2019; Lipatov et al. 2022). The excess of stars on the blue-bright side of the best-fitting CMD (Fig. 6a) strengthen the argument that the predicted rotation rates may be artificially too high due to missing or poorly modelled aspects of stellar rotation. We proposed a possible connection with the observed Be (Bastian et al. 2016; Milone et al. 2018) and UV-dim stars phenomenon (Martocchia et al. 2023; Milone et al. 2023b): a large fraction of fast rotators may develop decretion discs at high rotation rates, with dust grains forming in the outer regions (D'Antona et al. 2023; He et al. 2025) and absorbing light from stars seen close to equator-on, shifting their positions on the eMSTO. To explore this, we performed a schematic test in which we increased the reddening by $\Delta E(B-V) \sim 0.1$ mag for stars with $v/v_{\rm crit} \gtrsim 0.7$ observed within $\sim 15^\circ$ of the equatorial plane. This broadened the eMSTO while preserving realistic $v \sin i$ values and reducing the excess of blue-bright stars. While highly simplified, this experiment suggests that disc absorption could influence inferred rotation distributions. Testing this possibility will require both detailed disc modelling and more complete star-by-star spectroscopic and photometric data sets, including $v \sin i$ measurements across eMSTOs.

ACKNOWLEDGEMENTS

This project was undertaken with the assistance of resources and services from the National Computational Infrastructure (NCI), which is supported by the Australian Government. Access to NCI was supported by the University of Newcastle. HS is the recipient of an Australian Research Council Future Fellowship Award (project number FT220100330). This research is funded by this grant from the Australian Government. HS and LM acknowledge the Awabakal people, the traditional custodians of the unceded land on which their research was undertaken. AM acknowledges support from the ERC Consolidator Grant funding scheme (project ASTEROCHRONOMETRY, G.A. n. 772293 http://www.asterochronometry.eu). GB acknowledges fundings from the Fonds National de la Recherche Scientifique (FNRS) as a postdoctoral researcher. PE acknowledges support from the SNF grant No. 219745.

We thank the anonymous referee for the suggestions that led to a significant improvement of the quality of this work. We sincerely thank Léo Girardi for generously providing the reduced data for NGC 419 published in Girardi et al. (2009). LM thanks Diego Bossini for his help with bolometric corrections, Marco Tailo, Lorenzo Briganti, and Alessandro Mazzi for valuable discussions and suggestions. LM also gratefully acknowledges Georges Meynet, the STAREX group members, and the Observatoire de Genève for their warm hospitality during a research stay, where the idea for this work first took shape.

DATA AVAILABILITY

The MESA release r-24.03.1 used in this work is available at https://doi.org/10.5281/zenodo.10783349. The MESA SDK required to run the code is available at: https://doi.org/10.5281/zenodo.2603175. We have made the inlists and `run_star_extras.f90` used to generate the stellar models, publicly available on Zenodo: https://doi.org/10.5281/zenodo.15601753. The digital data underlying this article are available from the corresponding author upon reasonable request.

This work made use of the following software: PYTHON (https://www.python.org/), NUMPY (Harris et al. 2020), SCIPY (Virtanen et al. 2020), PANDAS (McKinney 2010; pandas development team T. 2020), MATPLOTLIB (Hunter 2007), PYGAD (Fawzy Gad 2021), MESA (Paxton et al. 2011, 2013, 2015, 2018, 2019; Jermyn et al. 2023), SYCLIST (Georgy et al. 2014), and TOPCAT (Taylor 2005).

REFERENCES

Abdurro’uf et al., 2022, ApJS, 259, 35
Aerts C., Mathis S., Rogers T. M., 2019, ARA&A, 57, 35
Amard L., Matt S. P., 2020, ApJ, 889, 108
Angulo C. et al., 1999, Nucl. Phys. A, 656, 3
Asplund M., Grevesse N., Sauval A. J., Scott P., 2009, ARA&A, 47, 481
Ball W. H., 2021, RNAAS, 5, 7
Bastian N., de Mink S. E., 2009, MNRAS, 398, L11
Bastian N., Niederhofer F., 2015, MNRAS, 448, 1863
Bastian N. et al., 2016, MNRAS, 465, 4795
Bastian N., Kamann S., Cabrera-Ziri I., Georgy C., Ekström S., Charbonnel C., de Juan Ovelar M., Usher C., 2018, MNRAS, 480, 3739
Beck P. G. et al., 2012, Nature, 481, 55
Bekki K., Mackey A. D., 2009, MNRAS, 394, 124
Beyer A. C., White R. J., 2024, ApJ, 973, 28
Bloecker T., 1995, A&A, 297, 727
Böhm-Vitense E., 1958, Z. Astrophys., 46, 108
Bossini D. et al., 2017, MNRAS, 469, 4718
Brandt T. D., Huang C. X., 2015, ApJ, 807, 25
Bressan A., Marigo P., Girardi L., Salasnich B., Dal Cero C., Rubele S., Nanni A., 2012, MNRAS, 427, 127
Brogaard K. et al., 2023, A&A, 679, A23
Casagrande L., VandenBerg D. A., 2018, MNRAS, 479, L102
Casamiquela L. et al., 2017, MNRAS, 470, 4363
Caughlan G. R., Fowler W. A., 1988, At. Data Nucl. Data Tables, 40, 283
Chaboyer B., Zahn J. P., 1992, A&A, 253, 173
Chen Y. et al., 2019, A&A, 632, A105
Chieffi A., Limongi M., 2013, ApJ, 764, 21
Choi J., Dotter A., Conroy C., Cantiello M., Paxton B., Johnson B. D., 2016, ApJ, 823, 102
Claret A., Torres G., 2017, ApJ, 849, 18
Cordoni G., Milone A. P., Marino A. F., Di Criscienzo M., D’Antona F., Dotter A., Lagioia E. P., Tailo M., 2018, ApJ, 869, 139
Cordoni G. et al., 2022, Nat. Commun., 13, 4325
Cordoni G. et al., 2024, MNRAS, 532, 1547
Cyburt R. H. et al., 2010, ApJS, 189, 240
D’Antona F. et al., 2023, MNRAS, 521, 4462
de Jager C., Nieuwenhuijzen H., van der Hucht K. A., 1988, A&AS, 72, 259
de Juan Ovelar M. et al., 2019, MNRAS, 491, 2129
Decressin T., Mathis S., Palacios A., Siess L., Talon S., Charbonnel C., Zahn J.-P., 2009, A&A, 495, 271
Dolphin A. E., 2002, MNRAS, 332, 91
Dotter A., 2016, ApJS, 222, 8
Dresbach F., Massari D., Lanzoni B., Ferraro F. R., Dalessandro E., Libralato M., Raso S., 2023, A&A, 679, A102
Dufton P. L., Lennon D. J., Villaseñor J. I., Howarth I. D., Evans C. J., de Mink S. E., Sana H., Taylor W. D., 2022, MNRAS, 512, 3331
Eggenberger P., Meynet G., Maeder A., Hirschi R., Charbonnel C., Talon S., Ekström S., 2008, Ap&SS, 316, 43
Eggenberger P., Miglio A., Montalban J., Moreira O., Noels A., Meynet G., Maeder A., 2010, A&A, 509, A72
Eggenberger P., Lagarde N., Charbonnel C., 2011, Impact of Rotational Mixing on the Global and Asteroseismic Properties of Red Giants. Springer, Berlin, p. 95
Eggenberger P., Montalbán J., Miglio A., 2012, A&A, 544, L4
Eggenberger P. et al., 2019, A&A, 621, A66
Ekström S., Meynet G., Maeder A., Barblan F., 2008, A&A, 478, 467
Elmegreen B. G., Efremov Y. N., 1997, ApJ, 480, 235
Endal A. S., Sofia S., 1976, ApJ, 210, 184
Endal A. S., Sofia S., 1978, ApJ, 220, 279
Espinosa Lara F., Rieutord M., 2011, A&A, 533, A43
Ettorre G. et al., 2025, MNRAS, 539, 2537
Fawzy Gad A., 2021, preprint (arXiv:2106.06158)
Ferguson J. W., Alexander D. R., Allard F., Barman T., Bodnarik J. G., Hauschildt P. H., Heffner-Wong A., Tamanai A., 2005, ApJ, 623, 585
Gaia Collaboration, 2018, A&A, 616, A1
Gaia Collaboration, 2021, A&A, 649, A1
Gaia Collaboration, 2023, A&A, 674, A1
Georgy C., Ekström S., Granada A., Meynet G., Mowlavi N., Eggenberger P., Maeder A., 2013, A&A, 553, A24
Georgy C., Granada A., Ekström S., Meynet G., Anderson R. I., Wyttenbach A., Eggenberger P., Maeder A., 2014, A&A, 566, A21
Girardi L., 1999, MNRAS, 308, 818
Girardi L., Groenewegen M. A. T., Weiss A., Salaris M., 1998, MNRAS, 301, 149
Girardi L., Mermilliod J. C., Carraro G., 2000, A&A, 354, 892
Girardi L., Rubele S., Kerber L., 2009, MNRAS, 394, L74
Girardi L., Eggenberger P., Miglio A., 2011, MNRAS, 412, L103

Girardi L. et al., 2013, MNRAS, 431, 3501
Girardi L., Costa G., Chen Y., Goudfrooij P., Bressan A., Marigo P., Bellini A., 2019, MNRAS, 488, 696
Glebbeek E., Gaburov E., de Mink S. E., Pols O. R., Portegies Zwart S. F., 2009, A&A, 497, 255
Gossage S. et al., 2019, ApJ, 887, 199
Goudfrooij P. et al., 2014, ApJ, 797, 35
Goudfrooij P., Girardi L., Correnti M., 2017, ApJ, 846, 22
Handberg R., Brogaard K., Miglio A., Bossini D., Elsworth Y., Slumstrup D., Davies G. R., Chaplin W. J., 2017, MNRAS, 472, 979
Harris C. R. et al., 2020, Nature, 585, 357
He C., Li C., Li G., 2025, ApJ, 979, 246
Heger A., Langer N., Woosley S. E., 2000, ApJ, 528, 368
Herwig F., 2000, A&A, 360, 952
Hidalgo S. L. et al., 2018, ApJ, 856, 125
Howarth I. D., 2011, MNRAS, 413, 1515
Hunt E. L., Reffert S., 2024, A&A, 686, A42
Hunter J. D., 2007, Comput. Sci. Eng., 9, 90
Hurley J., Tout C. A., 1998, MNRAS, 300, 977
Iglesias C. A., Rogers F. J., 1993, ApJ, 412, 752
Iglesias C. A., Rogers F. J., 1996, ApJ, 464, 943
Imbriani G. et al., 2005, Eur. Phys. J. A, 25, 455
Jermyn A. S. et al., 2023, ApJS, 265, 15
Kamann S. et al., 2018, MNRAS, 480, 1689
Kamann S. et al., 2020, MNRAS, 492, 2177
Kamann S. et al., 2023, MNRAS, 518, 1505
Kee N. D., Owocki S., Townsend R., Müller H. R., 2016, in Sigut T. A. A., Jones C. E., eds, ASP Conf. Ser. Vol. 506, Bright Emissaries: Be Stars as Messengers of Star-Disk Physics. Astron. Soc. Pac., San Francisco, p. 47
Khan S., Hall O. J., Miglio A., Davies G. R., Mosser B., Girardi L., Montalbán J., 2018, ApJ, 859, 156
Kippenhahn R., Thomas H. C., 1970, in Slettebak A., ed., Proc. IAU Colloq. 4: Stellar Rotation. Gordon and Breach Science Publishers, Oxford, p. 20
Kraft R. P., 1967, ApJ, 150, 551
Krumholz M. R., 2014, Phys. Rep., 539, 49
Kunz R., Fey M., Jaeger M., Mayer A., Hammer J. W., Staudt G., Harissopulos S., Paradellis T., 2002, ApJ, 567, 643
Langer N., 1998, A&A, 329, 551
Li C., de Grijs R., Deng L., 2014a, Nature, 516, 367
Li C., de Grijs R., Deng L., 2014b, ApJ, 784, 157
Li Z., Mao C., Zhang L., Zhang X., Chen L., 2016a, ApJS, 225, 7
Li C., de Grijs R., Bastian N., Deng L., Niederhofer F., Zhang C., 2016b, MNRAS, 461, 3212
Li C., Milone A. P., Sun W., de Grijs R., 2024, preprint (arXiv:2401.08062)
Lindegren L. et al., 2021, A&A, 649, A4
Lipatov M., Brandt T. D., Gossage S., 2022, ApJ, 934, 105
Maeder A., 2009, Physics, Formation and Evolution of Rotating Stars. Springer, Berlin
Maeder A., Meynet G., 2000, ARA&A, 38, 143
Maeder A., Zahn J.-P., 1998, A&A, 334, 1000
Majewski S. R. et al., 2017, AJ, 154, 94
Marino A. F., Przybilla N., Milone A. P., Da Costa G., D'Antona F., Dotter A., Dupree A., 2018a, AJ, 156, 116
Marino A. F., Milone A. P., Casagrande L., Przybilla N., nez L. B.-N., Criscienzo M. D., Serenelli A., Vilardell F., 2018b, ApJ, 863, L33
Marques J. P. et al., 2013, A&A, 549, A74
Martayan C., Baade D., Fabregat J., 2008, Proc. IAU Symp. 4, p. 349
Martocchia S., Bastian N., Saracino S., Kamann S., 2023, MNRAS, 520, 4080
McKinney W., 2010, in van der Walt S., Millman J., eds, Proc. 9th Python in Science Conference. p. 56
McSwain M. V., Gies D. R., 2005, ApJS, 161, 118
Metcalfe T. S. et al., 2020, ApJ, 900, 154
Meynet G., Maeder A., 1997, A&A, 321, 465
Miglio A. et al., 2012, MNRAS, 419, 2077
Milone A. P., Bedin L. R., Piotto G., Anderson J., 2009, A&A, 497, 755
Milone A. P. et al., 2018, MNRAS, 477, 2640
Milone A. P. et al., 2023a, MNRAS, 522, 2429
Milone A. P. et al., 2023b, MNRAS, 524, 6149
Molenda-Żakowicz J., Arentoft T., Frandsen S., Grundahl F., 2009, Acta Astron., 59, 69
Mucciarelli A., Minelli A., Lardo C., Massari D., Bellazzini M., Romano D., Origlia L., Ferraro F. R., 2023, A&A, 677, A61
Nandal D. et al., 2024, A&A, 684, A169
Nelder J. A., Mead R., 1965, Comput. J., 7, 308
Nguyen C. T. et al., 2022, A&A, 665, A126
Palacios A., Charbonnel C., Talon S., Siess L., 2006, A&A, 453, 261
pandas development team T., 2020, pandas-dev/pandas: Pandas, Zenodo, doi:10.5281/zenodo.3509134
Paxton B., Bildsten L., Dotter A., Herwig F., Lesaffre P., Timmes F., 2011, ApJS, 192, 3
Paxton B. et al., 2013, ApJS, 208, 4
Paxton B. et al., 2015, ApJS, 220, 15
Paxton B. et al., 2018, ApJS, 234, 34
Paxton B. et al., 2019, ApJS, 243, 10
Pinsonneault M. H., Kawaler S. D., Sofia S., Demarque P., 1989, ApJ, 338, 424
Porter J. M., Rivinius T., 2003, PASP, 115, 1153
Rivinius T., Carciofi A. C., Martayan C., 2013, A&AR, 21, 69
Royer F., Zorec J., Gómez A. E., 2007, A&A, 463, 671
Rubele S., Kerber L., Girardi L., 2010, MNRAS, 403, 1156
Salaris M., Cassisi S., 2017, R. Soc. Open Sci., 4, 170192
Salpeter E. E., 1954, Aust. J. Phys., 7, 373
Sandquist E. L. et al., 2020, AJ, 159, 96
Serenelli A. M., Basu S., 2010, ApJ, 719, 865
Skowron D. M. et al., 2021, ApJS, 252, 23
Slettebak A., 1988, PASP, 100, 770
Sun W., Li C., Deng L., de Grijs R., 2019, ApJ, 883, 182
Talon S., Zahn J. P., 1997, A&A, 317, 749
Taylor M. B., 2005, in Shopbell P., Britton M., Ebert R., eds, ASP Conf. Ser. Vol. 347, Astronomical Data Analysis Software and Systems XIV. Astron. Soc. Pac., San Francisco, p. 29
Townsend R. H. D., Owocki S. P., Howarth I. D., 2004, MNRAS, 350, 189
Trampedach R., Stein R. F., Christensen-Dalsgaard J. r., Nordlund Å., Asplund M., 2014, MNRAS, 442, 805
van Belle G. T., 2012, A&AR, 20, 51
van Saders J. L., Ceillier T., Metcalfe T. S., Silva Aguirre V., Pinsonneault M. H., García R. A., Mathur S., Davies G. R., 2016, Nature, 529, 181
Virtanen P. et al., 2020, Nat. Methods, 17, 261
von Zeipel H., 1924, MNRAS, 84, 684
Wang C. et al., 2023, A&A, 670, A43
Weaver T. A., Zimmerman G. B., Woosley S. E., 1978, ApJ, 225, 1021
Wu X., Li C., de Grijs R., Deng L., 2016, ApJ, 826, L14
Zahn J. P., 1992, A&A, 265, 115
Ziółkowska O., Smolec R., Thoul A., Farrell E., Rathour R. Singh, Hocdé V., 2024, ApJS, 274, 30

APPENDIX A: CALIBRATION OF THE DIFFUSION COEFFICIENTS TO MIMIC ROTATIONAL MIXING IN GENEC MODELS

In this section, we describe the method used to calibrate the fully diffusive custom rotational mixing prescription in MESA active during the MS phase implemented in `grid 2` models. This custom prescription is designed to mimic rotational mixing in GENEC models from Georgy et al. (2013) (hereafter referred to as the reference grid). The evolution of angular momentum and chemical element profiles, due to rotation-driven instabilities in MESA, is governed by two diffusion equations, which are computationally efficient to solve

$$\frac{\partial \Omega}{\partial t} = \frac{1}{\rho r^4}\frac{\partial}{\partial r}\left[\rho r^4 \left(D_{\rm mix}/f_c\right)\frac{\partial \Omega}{\partial r}\right], \tag{A1}$$

$$\frac{\partial X_i}{\partial t} = \frac{1}{\rho r^2}\frac{\partial}{\partial r}\left(\rho r^2 D_{\rm mix}\frac{\partial X_i}{\partial r}\right), \tag{A2}$$

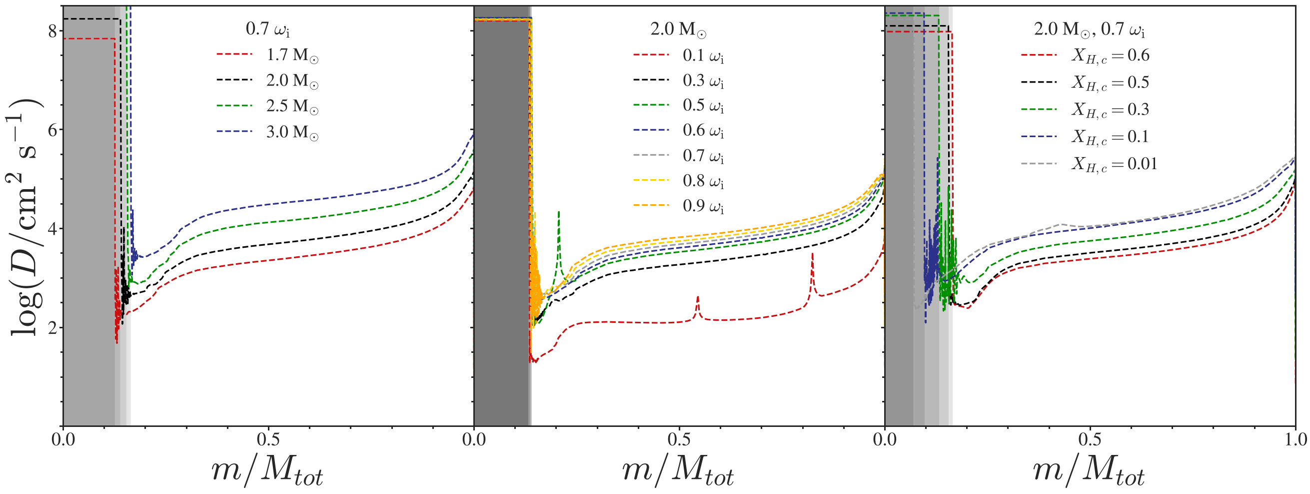

Figure A1. Left: $D_{\rm mix}$ profiles for GENEC models with masses of 1.7, 2.0, 2.5, and 3.0 M$_\odot$, each with an initial rotation rate of 0.7 ω, evaluated at approximately halfway through the MS phase ($X_{^1{\rm H,c}} = 0.35$). Centre: $D_{\rm mix}$ profiles for a 2.0 M$_\odot$ GENEC model with initial rotation rates of 0.1, 0.3, 0.5, 0.6, 0.7, 0.8, and 0.9 ω, evaluated at approximately halfway through the MS phase ($X_{^1{\rm H,c}} = 0.35$). Right: $D_{\rm mix}$ profiles for a 2.0 M$_\odot$ GENEC model with an initial rotation rate of 0.7 ω, evaluated at different evolutionary stages during the MS, corresponding to central hydrogen mass fractions of $X_{^1{\rm H,c}} = 0.6, 0.5, 0.3, 0.1, 0.01$.

where X_i is the mass fraction of nuclide i, $D_{\rm mix}$ is the total diffusion coefficient (a sum of all diffusion coefficients for the transport processes considered), and f_c is the ratio of the diffusion coefficient to the turbulent viscosity, defined as $f_c = D_{\rm mix}/\nu$. This ratio is calibrated using observational constraints. For details on the calculation of the diffusion coefficients associated with the transport processes in this diffusive formalism, see Heger et al. (2000).

The advective-diffusive formalism for rotation-induced mixing in GENEC (Eggenberger et al. 2008) describes angular momentum transport with an advective-diffusive equation

$$\rho \frac{d}{\mathrm{d}t}\left[r^2\Omega\right] = \frac{1}{5r^2}\frac{\partial}{\partial r}\left[\rho r^4 \Omega U\right] + \frac{1}{r^4}\frac{\partial}{\partial r}\left[\rho D_{\rm shear} r^4 \frac{\partial \Omega}{\partial r}\right], \tag{A3}$$

and chemical element transport with a diffusive equation

$$\begin{aligned}\rho \frac{\partial X_i}{\partial t} &= \frac{1}{r^2}\frac{\partial}{\partial r}\left[r^2 \rho \left(D_{\rm eff} + D_{\rm shear}\right)\frac{\partial X_i}{\partial r}\right] \\ &= \frac{1}{r^2}\frac{\partial}{\partial r}\left[r^2 \rho D_{\rm mix}\frac{\partial X_i}{\partial r}\right].\end{aligned} \tag{A4}$$

Here, U is the radial component of the meridional circulation velocity, $D_{\rm eff}$ is the effective diffusion coefficient for the transport of chemical elements due to the combined effects of meridional circulation and horizontal turbulence, and $D_{\rm shear}$ is the diffusion coefficient for the radial shear instability (for details see Eggenberger et al. 2008). The diffusion coefficients in the GENEC formalism are derived using self-consistent physical models based on reasonable assumptions (Maeder 2009; Nandal et al. 2024). These coefficients are complicated functions, depending on the local physical conditions within the star and the velocity of meridional circulation (see Chaboyer & Zahn 1992; Meynet & Maeder 1997; Maeder 2009, for details).

An inspection of the diffusion coefficients $D_{\rm mix}$ (see Fig. A1) across the range of masses and rotation rates covered by the reference grid, reveals that the qualitative shape of the diffusion coefficient profiles remains consistent despite the presence of some short-lived spikes. The most notable variation is that $D_{\rm mix}$ scales approximately by an overall factor that increases with stellar mass, initial rotation rate $\omega_{\rm i}$, and progression along the MS phase (see Fig. A1).

The goal of this custom rotational mixing prescription is not to exactly replicate the advective-diffusive implementation of GENEC models but rather to develop a computationally efficient approximation that qualitatively reproduces the main properties of GENEC rotating models relative to their non-rotating counterparts. Specifically, the aim is to reproduce the increase in MS lifetime and changes to the surface chemical element within a small tolerance. We consider the $D_{\rm mix}$ profile to consist of two distinct zones: the near-core zone, dominated by $D_{\rm eff}$, which accounts for the combined effects of meridional circulation and horizontal turbulence, and the envelope zone, dominated by $D_{\rm shear}$. The value of $D_{\rm mix}$ near the core primarily influences the MS lifetime and the increase in MS luminosity, whereas the value in the envelope mainly affects surface chemical element abundance variations. To approximate the total diffusion coefficient $D_{\rm mix}$ profile in the radiative zone, we adopt the following parametric function:

$$\Phi(q) = \begin{cases} \sigma \cdot \left[a \cdot q - (q_{\rm cc} + b) + 10^{c\cdot q - d} + 10^{e \cdot q - f}\right] & \text{if } \Phi > \beta, \\ \beta & \text{if } \Phi \leq \beta, \end{cases} \tag{A5}$$

where $q = m/M$, with m representing the mass within a given radius, M the total stellar mass and $q_{\rm cc}$ the mass coordinate of the convective core boundary, including the overshooting region. The parameters a, b, c, d, e, and f determine the shape of the function and are fixed via least-squares minimization to fit the $D_{\rm mix}$ profile of a representative model[4] (see Fig. A2).

The fitted parameter values are listed in Table A1.

We discuss the calibration constants, σ and β, further in this Appendix.

In the MESA models of `grid 2`, we define the total diffusion coefficient for chemical transport as

$$D_{\rm mix}(q) = \chi_{H,c} \cdot \Phi(q), \tag{A6}$$

---

[4] For calibration, we use a 2.0 M$_\odot$ model initialized with 0.7 $\omega_{\rm i}$ at the mid-point of the MS phase.

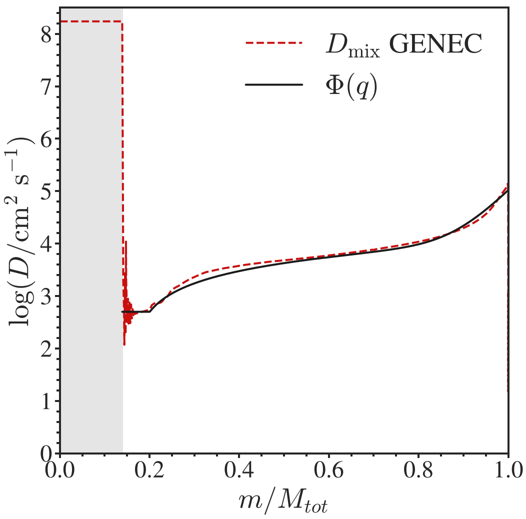

Figure A2. Best fit of the parametric function (equation A5) to the $D_{\rm mix}$ profile of the 2.0 $M_\odot$ model, selected as the representative model to determine the fixed shape parameters a, b, c, d, e, and f.

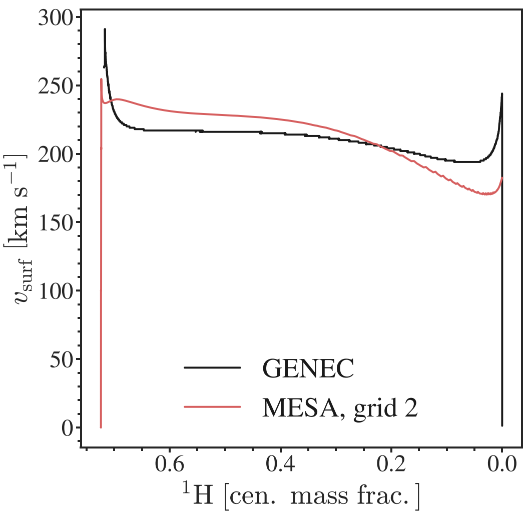

Figure A3. Comparison of the evolution of the equatorial velocity between a GENEC reference model (black) of 2.5 $M_\odot$, rotating with 0.8 $\omega_{\rm i}$, and a MESA model of the same mass and rotation rate from `grid 2` (red), calibrated using the technique described in Appendix A.

Table A1. Fixed parameters of the parametric function (equation A5) obtained through least squares minimization to fit the $D_{\rm mix}$ profile of a representative 2.0 $M_\odot$ model with an initial rotation rate of 0.7 ω.

Fixed parameter	Value
a	1.2480576095175386
b	0.0615015714089750
c	8.6996929817348025
d	8.0272056977252149
e	8.6995994374779517
f	8.0277869134778879

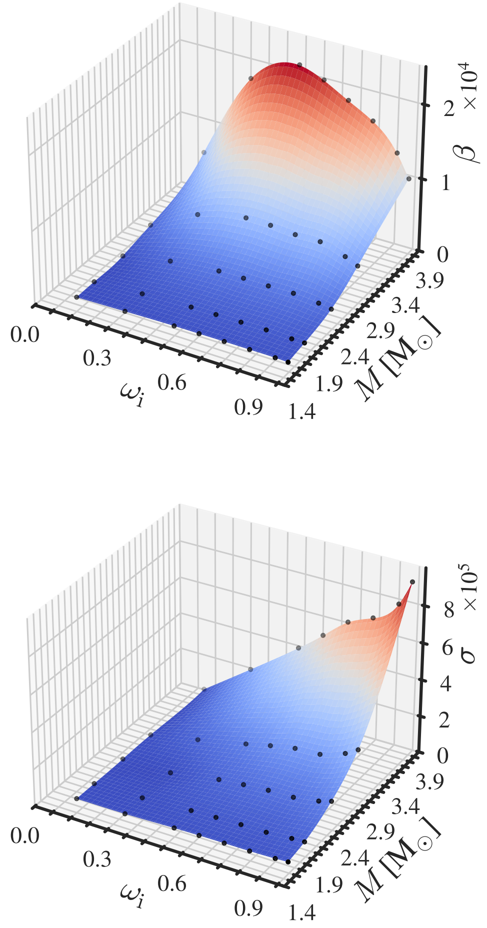

Figure A4. Top: Calibration results for the parameter β in solar metallicity models of `grid 2`. Bottom: Calibration results for the parameter σ in solar metallicity models of `grid 2`. In both panels, dots represent the calibrated values for the reference grid models, while the values of β and σ at intermediate points are obtained through cubic spline interpolation. Colour map reflects the value of β and σ, respectively.

and for the transport of angular momentum, we impose the angular momentum diffusion coefficient $\nu_{\rm AM}$ as

$$\nu_{\rm AM}(q) = 5 \cdot \chi_{H,c} \cdot \Phi(q), \tag{A7}$$

where $\chi_{H,c}$ is a factor that linearly increases from 0.01 to 1 over the MS phase, depending on the central hydrogen mass fraction. This approach qualitatively reproduces the overall increase in $D_{\rm mix}$ during the MS phase, consistent with trends observed in the GENEC models, as shown in the right panel of Fig. A1. The scaling factor of 5 applied to the angular momentum diffusion coefficient ensures a qualitatively acceptable match to the evolution of surface equatorial velocity across all GENEC models in the reference grid (Fig. A3).

Using a good approximation of GENEC $D_{\rm mix}$ values in MESA does not guarantee similar increases in MS lifetime or surface chemical element variations. This discrepancy arises from inherent differences in the codes and assumptions in their input physics. Consequently, we treat β and σ as free parameters to be calibrated in order to reproduce similar increases in MS lifetime and surface chemical element variations. These parameters scale the diffusion coefficients in the near-core and envelope zones, respectively, without altering their overall shape.

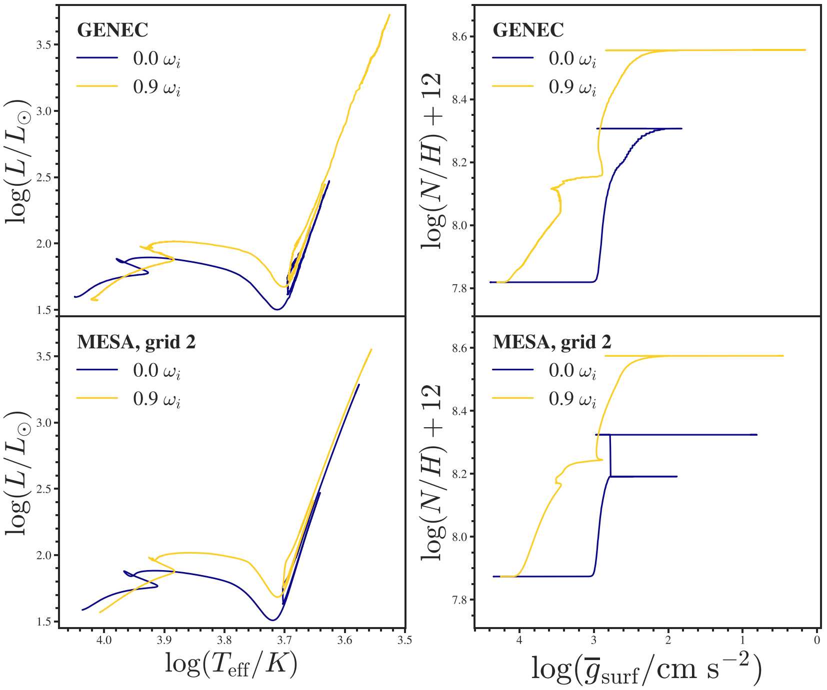

Figure A5. Left: Comparison of evolutionary tracks in the HR diagram for 2.5 $M_\odot$ stars from GENEC reference models (top) rotating at 0.9 $\omega_{\rm i}$ and non-rotating, and from MESA models (bottom) with the same mass and rotation rate, taken from `grid 2` and calibrated as described in Appendix A. Right: Comparison of the evolution of the surface nitrogen-to-hydrogen abundance ratio for 2.5 $M_\odot$ stars from GENEC reference models (top) rotating at 0.8 $\omega_{\rm i}$ and non-rotating, and from MESA models (bottom) from `grid 2`, calibrated using the same method.

We calibrated the profiles using the Nelder–Mead optimization algorithm (Nelder & Mead 1965), which minimizes the residuals of two *calibration parameters*, Π_1 and Π_2

$$\Pi_1 = \frac{\tau_{\rm TAMS}^{\omega_{\rm i}}}{\tau_{\rm TAMS}^{0.0}}, \tag{A8}$$

$$\Pi_2 = \frac{(X_{\rm N}/X_{\rm H})_{\rm TAMS}^{\omega_{\rm i}}}{(X_{\rm N}/X_{\rm H})_{\rm TAMS}^{0.0}}, \tag{A9}$$

where $\tau_{\rm TAMS}^{\omega_{\rm i}}$ and $(X_{\rm N}/X_{\rm H})_{\rm TAMS}^{\omega_{\rm i}}$ are the age and the surface nitrogen-to-hydrogen ratio, respectively, at the terminal age main sequence (TAMS) of the model with an initial rotation rate $\omega_{\rm i}$. The residuals to be minimized are

$$\Delta\Pi_1 = |\Pi_1^{\rm MESA} - \Pi_1^{\rm GENEC}|, \tag{A10}$$

$$\Delta\Pi_2 = |\Pi_2^{\rm MESA} - \Pi_2^{\rm GENEC}|. \tag{A11}$$

Calibration is considered successful when $\Delta\Pi_1 < 0.005$ and $\Delta\Pi_2 < 0.01$.Calibration is performed on solar metallicity ($Z = 0.014$) reference models from the Georgy et al. (2013) grid, spanning 1.7 to 4.0 $M_\odot$ and $0.1 \leq \omega_{\rm ini} \leq 0.95$. To compute models at intermediate masses, we interpolate the calibrated diffusion coefficients using a cubic spline. Fig. A4 presents the calibrated values of β and σ for the reference models (black dots) along with interpolated values. For masses below the lower limit of 1.7 $M_\odot$ (down to 1.4 $M_\odot$), we linearly extrapolate the calibrated diffusion coefficients using the slope of the cubic spline at 1.7 $M_\odot$. However, due to this extrapolation, conclusions should be avoided for masses below 1.7 $M_\odot$. For lower metallicities, we adopt the same calibrated values as at solar metallicity, since Georgy et al. (2013) found only a very weak dependence of the diffusion coefficients on Z.

We activated this custom implementation of rotation-induced mixing during the MS phase and, at TAMS, gradually transitioned over 500 time-steps, to the default implementation. Notably, GENEC models also transition to a fully diffusive implementation after the MS phase (Nandal et al. 2024). With this calibration, we achieve a good approximation of the key properties of rotating GENEC models using MESA. By construction, main-sequence lifetimes and surface chemical abundance variations are well reproduced (see right panel of Fig. A5). In addition, the evolution in the HR diagram and the equatorial velocity are reasonably well reproduced, as shown in the left panel of Fig. A5 and in Fig. A3. In Fig. A5, we compare 2.5 $M_\odot$ models, which are the lowest-mass GENEC models that include the helium-burning phase.

APPENDIX B: PROCESSING EVOLUTIONARY TRACKS TO CREATE A UNIFORM BASIS FOR INTERPOLATION

The evolutionary tracks of `grid 1` and `grid 2` are processed using a method closely following that described in Dotter (2016), but adapted to the SYCLIST format. This method is based on 'equivalent evolutionary points' (EEPs, see Dotter 2016), a series of points that can be identified across all stellar evolutionary tracks. We define eight primary EEPs as follows:

(i) ZAMS: the first point after the H-burning luminosity that exceeds 99.9 per cent of the total luminosity and before the central H mass fraction decreases by 0.0015 from its initial value.

(ii) Coolest point of the MS: the point at the lowest temperature before the central H mass fraction falls below $1.7 \cdot 10^{-4}$.

(iii) Turn-off: the hottest point between point 2 and the point when the central H mass fraction falls below $1 \cdot 10^{-10}$.

(iv) RGB base: the lowest luminosity point in the post-MS phase (after point 3).

Table B1. Number of secondary EEPs in each segment of the evolutionary track.

Segment	Secondary EEPs
1–2	80
2–3	30
3–4	50
4–5	50
5–6	40
6–7	90
7–8	60

(v) RGB tip: the highest luminosity point after point 4 and before the centre becomes convective due to He burning.

(vi) Start of the stable Core Helium Burning: the minimum luminosity of the Core Helium Burning phase.

(vii) End of Core Helium Burning: the first point after point 6 when convection due to He burning in the centre stops.

(viii) First thermal pulse: the end of the evolutionary track.

Between the primary EEPs, we defined secondary EEPs (Table B1) to accurately capture the morphology of each segment of the evolutionary track. The method adopted is identical to that described in Section 2.2 of Dotter (2016). At the low- and high-mass ends of the mass range covered by our grid, some of the primary EEPs can no longer be defined. In these cases, we omit the corresponding primary EEP and instead fill the interval with the same number of secondary EEPs.

In the left panel of Fig. B1, we compare 1 Gyr non-rotating isochrones computed using models from `grid 1` (top left) and `grid 2` (bottom left) with non-rotating isochrones from the GENEC (Georgy et al. 2013), PARSEC V2.0 (Nguyen et al. 2022), MIST (Choi et al. 2016), and BASTI (Hidalgo et al. 2018) data bases. The `grid 1` non-rotating isochrone is consistent with those from the other data bases. In contrast, the GENEC models exhibit a significantly fainter MSTO due to the smaller convective core overshooting adopted. Note the close agreement between the `grid 2` and GENEC isochrones, as intended.

In the right panel of Fig. B1, we show a comparison between non-rotating and rotating 1 Gyr isochrones computed using models from `grid 1` (top) and `grid 2` (bottom), alongside the corresponding rotating isochrones from GENEC (Georgy et al. 2013) and PARSEC V2.0 (Nguyen et al. 2022). Note that here we use the theoretical definitions of L and $T_{\rm eff}$, not the observationally derived quantities $L_{\rm MES}$ and $T_{\rm eff,MES}$.

The rotating GENEC isochrone (and, by construction, that from `grid 2`) is hotter and more luminous than the rotating PARSEC V2.0 isochrone, which in turn is hotter and more luminous than that from `grid 1`. This reflects the increasing strength of rotational mixing in the GENEC, PARSEC V2.0, and `grid 1` models, respectively.

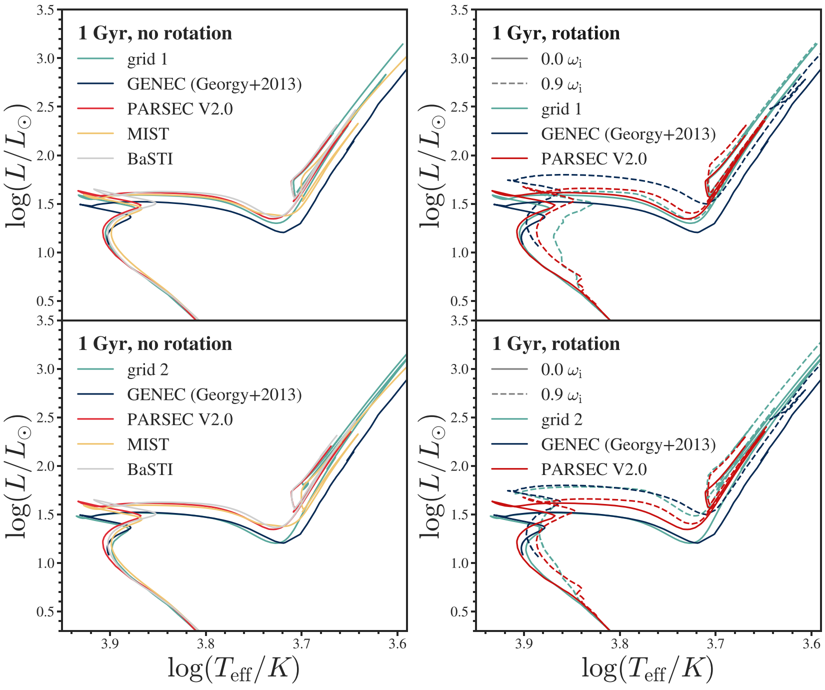

Figure B1. Left: Non-rotating 1 Gyr isochrones at $Z = 0.010$ from `grid 1` (top, green) and `grid 2` (bottom, green), compared with GENEC (Georgy et al. 2013) (blue), PARSEC V2.0 (Nguyen et al. 2022) (red), MIST (Choi et al. 2016) (yellow), and BASTI (Hidalgo et al. 2018) (grey). The fainter MSTO in GENEC reflects its smaller core overshooting. Note the close match between `grid 2` and GENEC, as intended. Right: 1 Gyr isochrones at $Z = 0.010$ for non-rotating (solid) and rotating ($\omega_{\rm i} = 0.9$, dashed) models from `grid 1` (top, green) and `grid 2` (bottom, green), compared with GENEC (blue) and PARSEC V2.0 (red). The rotating isochrones appear progressively hotter and more luminous from `grid 1` to PARSEC V2.0 to GENEC, reflecting the increasingly efficient rotational mixing adopted in each set of models.

This paper has been typeset from a TEX/LATEX file prepared by the author.